Talin tension sensor reveals novel features of focal adhesion force transmission and mechanosensitivity

Abhishek Kumar,[1] Mingxing Ouyang,[1] Koen Van den Dries,[1] Ewan James McGhee,[2] Keiichiro Tanaka,[1] Marie D. Anderson,[3] Alexander Groisman,[4] Benjamin T. Goult,[3] Kurt I. Anderson,[2] and Martin A. Schwartz[1,5,6]

[1]Yale Cardiovascular Research Center, Cardiovascular Medicine, Department of Internal Medicine, Yale School of Medicine, Yale University, New Haven, CT 06511
[2]Beatson Institute for Cancer Research, Glasgow G20 0TZ, Scotland, UK
[3]School of Biosciences, University of Kent, Canterbury CT2 7NZ, England, UK
[4]Department of Physics, University of California, San Diego, La Jolla, CA 92093
[5]Department of Cell Biology and [6]Department of Biomedical Engineering, Yale University, New Haven, CT 06520

Integrin-dependent adhesions are mechanosensitive structures in which talin mediates a linkage to actin filaments either directly or indirectly by recruiting vinculin. Here, we report the development and validation of a talin tension sensor. We find that talin in focal adhesions is under tension, which is higher in peripheral than central adhesions. Tension on talin is increased by vinculin and depends mainly on actin-binding site 2 (ABS2) within the middle of the rod domain, rather than ABS3 at the far C terminus. Unlike vinculin, talin is under lower tension on soft substrates. The difference between central and peripheral adhesions requires ABS3 but not vinculin or ABS2. However, differential stiffness sensing by talin requires ABS2 but not vinculin or ABS3. These results indicate that central versus peripheral adhesions must be organized and regulated differently, and that ABS2 and ABS3 have distinct functions in spatial variations and stiffness sensing. Overall, these results shed new light on talin function and constrain models for cellular mechanosensing.

Introduction

Integrins connect the ECM to the actin cytoskeleton through a complex set of linkages in which the cytoskeletal protein talin plays a prominent role (Ziegler et al., 2008; Calderwood et al., 2013). The N-terminal FERM (or head) domain of talin binds directly to integrin β subunit cytoplasmic domains and is required for conformational activation of integrins to bind ECM proteins with high affinity. Talin contains three F-actin–binding sites (ABSs), with the far C-terminal–binding site in the rod domain, ABS3, generally thought to be the most important. The talin rod domain also contains multiple binding sites for vinculin, which are buried within 4- and 5-α-helical bundles. When talin is under mechanical tension, these domains can unravel to allow binding of the vinculin head domain, which reinforces the linkage to actin through an ABS in the vinculin tail. Talin deletion in several organisms yields phenotypes that are similar to deletion or mutation of the integrins themselves, consistent with its essential role (Monkley et al., 2000; Brown et al., 2002; Cram et al., 2003).

The mechanosensitivity of integrin-mediated adhesions allows tissues to tune their function and gene expression to mechanical cues in the environment (Orr et al., 2006; Costa et al., 2012). For example, cells sense the mechanical stiffness of the ECM and modulate their own contractility, signaling, and gene expression programs accordingly, a property termed stiffness sensing (Humphrey et al., 2014). These effects include modulation of ECM production by matrix stiffness and externally applied forces. Mechanosensing through integrins is important in development and numerous diseases including cancer, hypertension, and fibrosis (Orr et al., 2006; Butcher et al., 2009).

The force-transmitting linkages between integrins and actin are dynamic, with F-actin flowing over the adhesions under the force exerted by both actin polymerization and myosin-dependent filament sliding (Case and Waterman, 2015). In focal adhesions (FAs) near cell edges, actin flows rearward over the immobile integrins, with talin and vinculin moving rearward at intermediate rates. The integrin- and F-actin bonds between vinculin and talin must therefore be dynamic, with rapid association and dissociation, to mediate force transmission, the so-called FA clutch. How this dynamic assembly mediates mechanotransduction is therefore a key question.

Development of a method to measure forces across specific molecules using a fluorescence resonance energy transfer (FRET) pair connected to a calibrated spring demonstrated directly that vinculin in FAs is under mechanical tension (Grashoff et al., 2010). In the present study, we developed a talin tension

Correspondence to Martin A. Schwartz: martin.schwartz@yale.edu

Abbreviations used in this paper: ABS, actin-binding site; CS, control sensor; FA, focal adhesion; FLIM, fluorescence lifetime imaging microscopy; FRET, fluorescence resonance energy transfer; LPA, lysophosphatidic acid; PDMS, polydimethylsiloxane; RIPA, radioimmunoprecipitation assay; TCSPC, time-correlated single photon counting; TS, tension sensor; VBS, vinculin-binding site.

Supplemental material can be found at:
http://doi.org/10.1083/jcb.201510012

The Rockefeller University Press $30.00
J. Cell Biol. Vol. 213 No. 3 371–383
www.jcb.org/cgi/doi/10.1083/jcb.201510012

sensor (TS) and explored the role of mechanical force across talin in integrin-mediated adhesion and mechanotransduction.

Results

Construction and characterization of a talin TS

We previously developed a FRET-based TS module consisting of a donor fluorophore connected to an acceptor via a nanospring derived from the elastic spider silk protein flagelliform (Grashoff et al., 2010). In the absence of tension, the nanospring is compact and FRET is high; application of tension stretches the spring and decreases FRET (Fig. 1 A). Here, we used a sensor module with the same nanospring connecting EGFP as donor and tagRFP as acceptor. Talin consists of a head domain that directly binds β integrin tails and a rod domain that binds F-actin both directly through ABSs and indirectly through vinculin-binding sites (VBSs). There are three ABSs, with the C-terminal ABS3 generally thought to be the most important. Hence, the TS module was inserted into a flexible sequence in between the head and the rod domains (Fig. 1 B, talin-TS). A control sensor (CS) was also designed with the module attached at the C terminus, with a short linker to avoid disrupting dimerization and the nearby ABS3 (Fig. 1 B, talin-CS).

Both talin-CS and talin-TS constructs were transfected into talin1$^{-/-}$ fibroblasts. Western blotting for either GFP or talin demonstrated expression of both proteins at the expected size (Fig. 1 C and Fig. S1, A and B). We noticed that in some experiments, talin-TS showed some additional bands (Fig. S1, A and C) suggestive of degradation, consistent with talin's known sensitivity to calpain (Beckerle et al., 1987). These additional bands were not detected when probed with anti-GFP (Fig. S1 B), whereas a band of ∼85 kD was present in the GFP Western blots, consistent with the larger fragments containing the talin head plus the TS module. Addition of calpain inhibitors substantially reduced the appearance of fragments (Fig. S1 D). When the cells were briefly cell extracted with a cytoskeletal-stabilizing, mild detergent buffer (Plopper and Ingber, 1993), the additional bands were largely soluble (Fig. S1 E). Together, these observations suggest that calpain fragments of talin-TS are present but mainly cytoplasmic.

The sensors localized efficiently at FAs marked by paxillin, with some present in the cytosol (Fig. 1 D). Photobleaching small regions within FAs showed that talin-TS and talin-CS had exchange dynamics and mobile fractions similar to a previously characterized N-terminal EGFP talin (Fig. 1 E; Kopp et al., 2010). Furthermore, FA turnover, both assembly and disassembly, was not affected by talin-TS, measured by paxillin EGFP as an independent marker of FA (Fig. S1, F–H). To test function, we examined cell spreading, which requires talin (Monkley et al., 2000). Talin1$^{-/-}$ fibroblasts (Fig. S1 I), however, up-regulate talin2 (Fig. S1 J), which partially rescues the cell spreading defect (Zhang et al., 2008). We therefore expressed talin-TS in talin1$^{-/-}$ fibroblasts with and without depletion of talin2 using the previously validated siRNA sequence from Zhang et al. (2008) (by ∼85%; Fig. 1 F). Expression of talin-TS increased spreading of talin1$^{-/-}$ cells and rescued the defect after talin2 knockdown (Fig. 1 G, quantified in H), a result that also supports specificity of the talin2 siRNA. Together, these results indicate that talin-TS is functional in cell adhesion and spreading.

To determine the tension on talin, we measured the FRET index in live cells as an approximation of FRET/molecule (Grashoff et al., 2010). This method measures FRET intensity, subtracts the background and the bleed through for the two fluorophores, and then normalizes to acceptor intensity. For these experiments, we analyzed FAs >0.25 μm^2, as smaller adhesions are harder to identify and quantify. In cells plated on fibronectin, FRET for talin-TS within FAs was low compared with talin-CS (Fig. 2, A and B). In contrast, when cells were plated on poly-L-lysine, where talin does not localize to FAs, FRET was high for both talin-TS and CS (Fig. 2, C and D). To check whether the talin-TS is sensitive to conformational changes associated with talin activation, we took advantage of the fact that talin recruitment to membranes is dependent on its conformational opening (Lagarrigue et al., 2015). Thus, membrane-bound talin outside of adhesive areas should be activated but without tension. Cells plated on polylysine show a clear rim of membrane-bound talin against the diffuse cytoplasmic pool. Membrane-bound versus cytoplasmic talin in cells on polylysine, at a plane well above the coverslip, showed no difference in FRET index (Fig. S2, A and B). Additionally, when FRET efficiency was measured in cell lysates by fluorimetry (Grashoff et al., 2010), talin-TS and CS were equivalent (Fig. 2 E). FRET index for talin-TS was similar in 3T3 cells that expressed endogenous talin (Fig. S2, C and D), indicating that the method is applicable to other cell types. Together, these data show that talin in FAs is under tension.

As an additional control, we tested whether tension on talin requires actomyosin contractility. Treating cells with blebbistatin at high doses and for long times disassembles FAs (Hotulainen and Lappalainen, 2006); thus cells were observed immediately after addition of a moderate dose (5 μM). We observed FA disassembly over ∼15 min, with a decrease of tension on talin over the same period (Fig. 2, F and G; and Fig. S1 E). Talin-CS showed no change in FRET index (Fig. S2 F). Conversely, increasing myosin II activity by lysophosphatidic acid (LPA) treatment of starved cells (Ridley and Hall, 1992) decreased the FRET index, indicating increased tension (Fig. S2, G and H). Thus, talin-TS reports myosin-dependent tension in FAs.

To confirm these data, we measured FRET efficiency by two additional methods. First, we performed acceptor photobleaching, which increases donor fluorescence proportionally to FRET efficiency (Karpova et al., 2003). To avoid complications from exchange of talin in FAs with the cytosolic pool, this was done in fixed cells; control experiments showed that fixation had no significant effect on FRET index (Fig. S2, I and J). Measurement of EGFP (donor) intensity showed an increase in donor fluorescence after tagRFP (acceptor) bleaching (Fig. S2 K). Quantifying these results for FRET efficiency per pixel within FAs showed lower FRET for talin-TS in FAs compared with talin-CS (Fig. S2 L). Thus, a second imaging method shows that talin in FAs is under tension. Lastly, we performed fluorescence lifetime imaging microscopy (FLIM), which has the added advantage that multiple lifetimes within single pixels can be determined. This approach yielded similar results (Fig. 2 H) with no evidence for multiple lifetimes (Fig. S2 M). As presented below, frequency domain measurement of fluorescence lifetime provided additional confirmation (Fig. 5 F). Thus, four different imaging modalities for talin-TS and comparison with a multiplicity of controls demonstrated low FRET in FAs, indicating that talin is under tension.

For molecules in multimers or clusters, intermolecular FRET can complicate the analysis of intramolecular FRET.

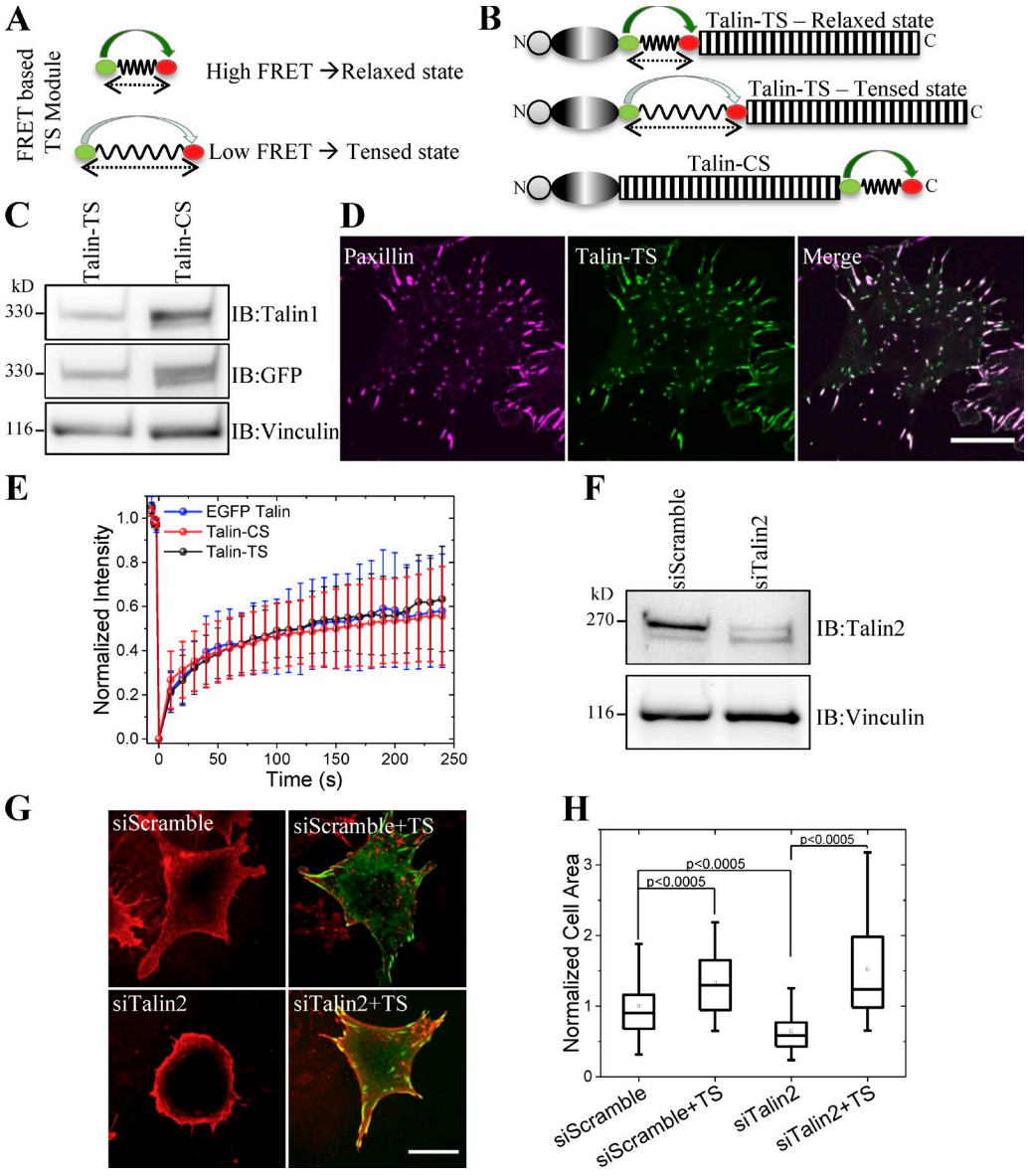

Figure 1. **Construction and characterization of a talin-TS.** (A) Schematic of the TS module in the relaxed (top) and tensed (bottom) states. (B) Schematic of talin-TS in the relaxed (top) and tensed (middle) state and the C-terminal, zero-tension control talin-CS (bottom). (C) Western blot for talin-TS and talin-CS in talin1$^{-/-}$ cells, probed for talin1 and vinculin, and stripped and reblotted with anti-GFP. (D) Localization of talin-TS in FAs marked by paxillin immunostaining. (E) FRAP of EGFP-talin (n = 38), talin-CS (n = 62), and talin-TS (n = 43) in FAs. Error bars are standard deviations. (F) Western blot of talin1$^{-/-}$ cells for talin2 after scrambled or talin2 siRNA transfection. (G) Spreading of talin1$^{-/-}$ cells with and without transfection of talin-TS and scrambled or talin2 siRNA. Cells were stained with Alexa Fluor 488–conjugated wheat germ agglutinin (red) to determine the cell area; talin-TS–positive cells are shown in green. (H) Normalized cell area for siScrambled (n = 99)-, siTalin2 (n = 107)-, and talin-TS–transfected cells (n = 50 for siScrambled+TS and n = 55 for siTalin2+TS). Bottom and top error bars represent 5th and 95th percentiles, respectively. Small rectangles in the box plots indicate means normalized to the control cells (scrambled siRNA, without talin-TS). Bars, 20 µm.

To measure intermolecular FRET for talin-TS, we made two constructs in which EGFP or tagRFP were mutated to abolish their fluorescence (Fig. S2 N). When cotransfected into cells, any FRET must therefore be intermolecular (Fig. S2, O and P). Treatment with blebbistatin to induce FA disassembly reduced intermolecular FRET in FAs by ∼25% (Fig. S2 Q). Thus, within FAs, intermolecular FRET is ∼20% of intramolecular FRET but is only slightly dependent on tension (∼25% decrease when tension is decreased) and in the opposite direction from intramolecular FRET. The net effect is that talin-TS measurements may slightly underestimate tension on talin, but the error is small.

Spatial variations in talin tension

Although the aforementioned analysis focused on FAs, we also analyzed the fluorescence signal from regions of the basal surface outside FAs. These data showed that FRET index for talin-TS was intermediate between the high value for talin under zero tension (e.g., cytoplasmic talin or talin-CS) and talin-TS in FAs (Fig. S2 R). Thus, some of the talin outside large FAs appears to be engaged with integrins and under tension. We noticed that FAs near cell edges (peripheral FAs) had consistently lower FRET index and higher tension than FAs near the nucleus (central FAs; Fig. 3, A and B). Peripheral FAs were larger compared with central FAs (Fig. S2 S); however, there was no

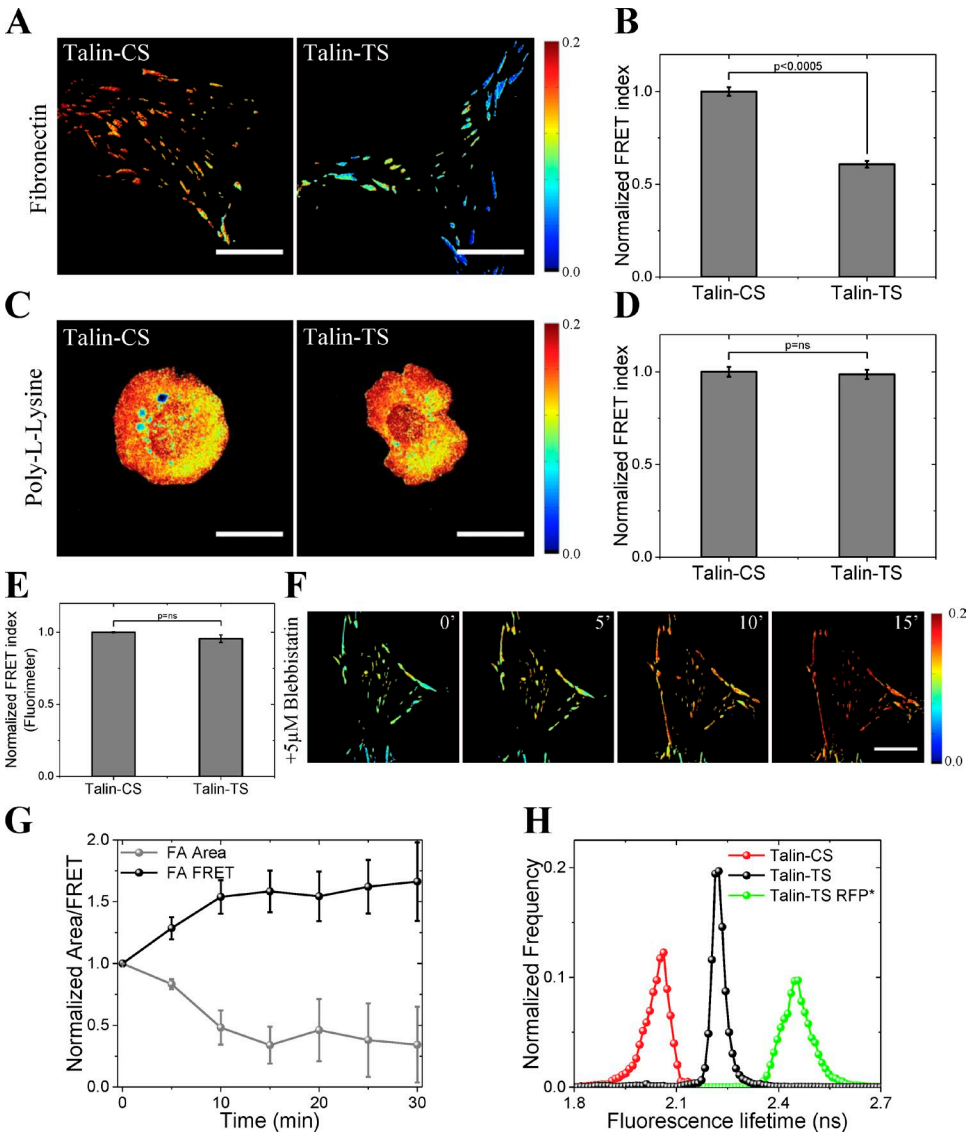

Figure 2. **Tension on talin requires actomyosin contractility.** (A) Pseudocolor map of FRET index for talin-CS and talin-TS within FAs of live cells on fibronectin. (B) Normalized FRET index for talin-CS (n = 30) and talin-TS (n = 32) within FAs. (C) FRET map of talin-CS and talin-TS in cells on 0.1% (wt/vol) poly-L-lysine–coated dishes. (D) Normalized FRET index of talin-CS (n = 20) and talin-TS (n = 15) from C. Error bars represent SEM. (E) Fluorimetric measurement of FRET for talin-CS and talin-TS in 293T cell lysates. n = 3. Error bars indicate standard deviation. (F) FRET map image time series of talin-TS after 5 µM blebbistatin treatment. (G) Plot of FA area and mean FRET index with time after blebbistatin treatment (n = 8). Error bars are standard deviations. (H) Histogram of time domain fluorescence lifetime measurement of EGFP in talin-TS, with mutated, nonfluorescent tagRFP and talin-CS as controls that indicate zero and maximal FRET (corresponding to maximal and minimal lifetimes), respectively. n > 60 each. The asterisk indicates a nonfluorescent mutant. (A, C, and F) Bars, 20 µm.

correlation between FA area and FRET index (Fig. S2, T and U) or talin intensity (Fig. S2, V and W) in either class of FAs. Furthermore, the mean talin intensity in peripheral FAs was similar to the central ones (Fig. S2 X) with no correlation between talin intensity and FRET index (Fig. S2, Y and Z); thus, tension on talin is independent of total talin in FAs.

Central FAs are connected by short actin stress fibers that go under the nucleus, whereas peripheral FAs are connected by long stress fibers that often go over the nucleus (Fig. S3 A; Kim et al., 2012; Li et al., 2014). Previous studies found that FA localization of zyxin is tension dependent, as is phosphorylation of paxillin on tyrosines 31 and 118 (Chrzanowska-Wodnicka and Burridge, 1996; Lele et al., 2006; Hirata et al., 2008; Pasapera et al., 2010). Indeed, these markers showed lower levels in central FAs (Fig. S3, B–D), whereas total paxillin (Fig. S3 E) and integrin β1 were similar (Fig. S3, F and G). There was no correlation between mean integrin β1 intensity and either FA area (Fig. S3, H and I) or mean FRET index (Fig. S3, J and K). Conversely, in cells plated on fibronectin for 24 h, fibronectin and tensin1 stains were stronger in FAs near the nucleus compared with the cell periphery (Fig. S3, L–N).

Unlike integrin α5β1, integrin αvβ3 was present mainly in peripheral FAs (Fig. S4 A) as reported previously (Schiller et al., 2013). We therefore checked whether the higher tension on talin in peripheral FAs is caused by the differential spatial engagement of integrin αvβ3. 3T3 cells, which express higher levels of αvβ3 than the talin1$^{-/-}$ cells (Fig. S4 B), showed a similar difference between central and peripheral adhesions and thus were used for these experiments. Addition of cyclic RGD, which inhibits αvβ3 but not α5β1, unexpectedly induced

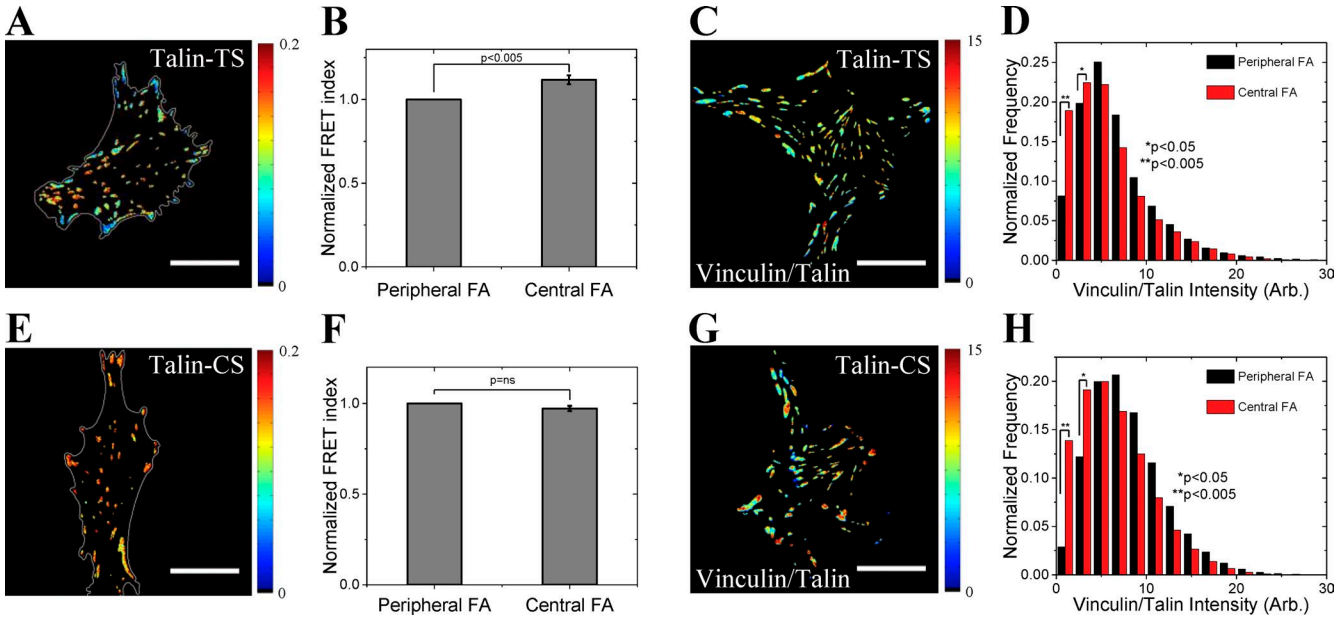

Figure 3. **Spatial variation in talin tension within single cells.** (A and E) Pseudocolor map of FRET index for talin-TS (A) and for talin-CS (E) within FAs of cells plated on fibronectin-coated dishes with cell boundaries drawn in white. (B and F) Normalized FRET index in central and peripheral FAs for talin-TS (n = 32; B) and for talin-CS (n = 30; F). Error bars represent SEM. (C and G) Vinculin/talin intensity ratio map for talin-TS (C)– and for talin-CS (G)–transfected talin1$^{-/-}$ cells fixed and stained for vinculin. (D and H) Histograms of pixel-wise vinculin/talin intensity ratio for talin-TS cells (n = 25; D) and for talin-CS (n = 30; H). Bars, 20 µm. Arb., arbitrary units.

a modest increase in tension on talin (Fig. S4, C and D) but did not diminish the difference between central and peripheral adhesions (Fig. S4, E and F). The reason for the increase in tension after addition of RGD is unknown. However, the results show that differential integrin utilization does not mediate the spatial heterogeneity. Although vinculin is also under tension in FAs and directly binds to talin, we found that the vinculin to talin intensity ratio was very slightly higher in central versus peripheral FAs (Fig. 3, C and D; and Fig. S3 O). The talin-CS control did not show any spatial variation in tension between peripheral and central FAs (Fig. 3, E and F) while maintaining similar vinculin distribution (Fig. 3 G and H). Thus, tension on talin is lower in central adhesions with characteristics of fibrillar adhesions (Zamir et al., 1999).

Mechanosensing

Cells on substrates of low rigidity reduce their myosin activity and exert lower traction forces, coincident with forming smaller adhesions (Wang et al., 2000; Balaban et al., 2001), though the decrease in FA size may not compensate for the reduced force under all conditions (Beningo et al., 2001). How cells sense substrate rigidity and decrease traction force is a major unanswered question. To investigate this effect at the level of talin tension, cells transfected with talin-TS or CS were plated on fibronectin-coated polydimethylsiloxane (PDMS) gels at ∼3 kPa or ∼30 kPa, the range over which fibroblasts respond to substrate stiffness (Solon et al., 2007). Cells on substrates of variable stiffness showed a transition in cell morphology between 3 and 30 kPa, a characteristic of stiffness sensing (Fig. S4, G and H). We observed consistently lower force on talin on substrates of low rigidity (Fig. 4 A), whereas talin-CS showed no difference (Fig. 4 B). Substrate stiffness did not alter the ratio of integrin β1 to talin within the FAs (Fig. S4, I–M), nor did talin FRET index show any dependence on integrin β1 intensity (Fig. S4, N–R). Next, we examined vinculin tension in this system. Remarkably, tension across vinculin was completely independent of substrate rigidity (Fig. 4, C and D). A wider range of stiffnesses gave similar results (Fig. S5, A–F). These results indicate that talin must be part of the rigidity-sensing mechanism, whereas its direct binding partner vinculin is buffered from these effects and thus must be positioned downstream of the sensing mechanism.

Role of VBSs and ABSs in regulating force on talin

Talin connects to actin filaments through multiple ABSs and VBSs. We first investigated the role of vinculin in force transmission by transfecting talin-TS into vinculin$^{-/-}$ cells and by transfecting talin1$^{-/-}$ cells with two different siRNA sequences to vinculin (Fig. 5, A and B). Talin-TS remained localized to FAs, as expected (Volberg et al., 1995). Both methods to reduce vinculin expression moderately reduced force on talin, with a somewhat larger effect in the null cells where vinculin was completely absent (Fig. 5 C and Fig. S5 G). Thus, vinculin contributes to force on talin.

Earlier studies focused on ABS3 near the talin C terminus (Gingras et al., 2008; Srivastava et al., 2008; Franco-Cea et al., 2010), which is generally pictured as the main direct connection to actin filaments (Puklin-Faucher and Sheetz, 2009; Wehrle-Haller, 2012). Hence, three point mutations (K2443D, V2444D, and K2445D) that reduce actin binding at ABS3 by ∼75% (Gingras et al., 2008) were introduced into talin-TS. This mutated construct showed normal localization to FAs (Fig. S5 H) and a similar FRET index compared with wild-type talin-TS (Fig. 5, D and E). Tension was also blebbistatin sensitive (Fig. S5 I). Talin-TS and ABS3-mutated TS also had similar levels of vinculin in FAs (Fig. S5 J). Thus, Talin ABS3 is dispensable for force transmission.

We therefore sought to test ABS2, which comprises domains R4–R8 in the middle of the rod domain (Fig. S5, K and L). We found that mutating four conserved residues in this site

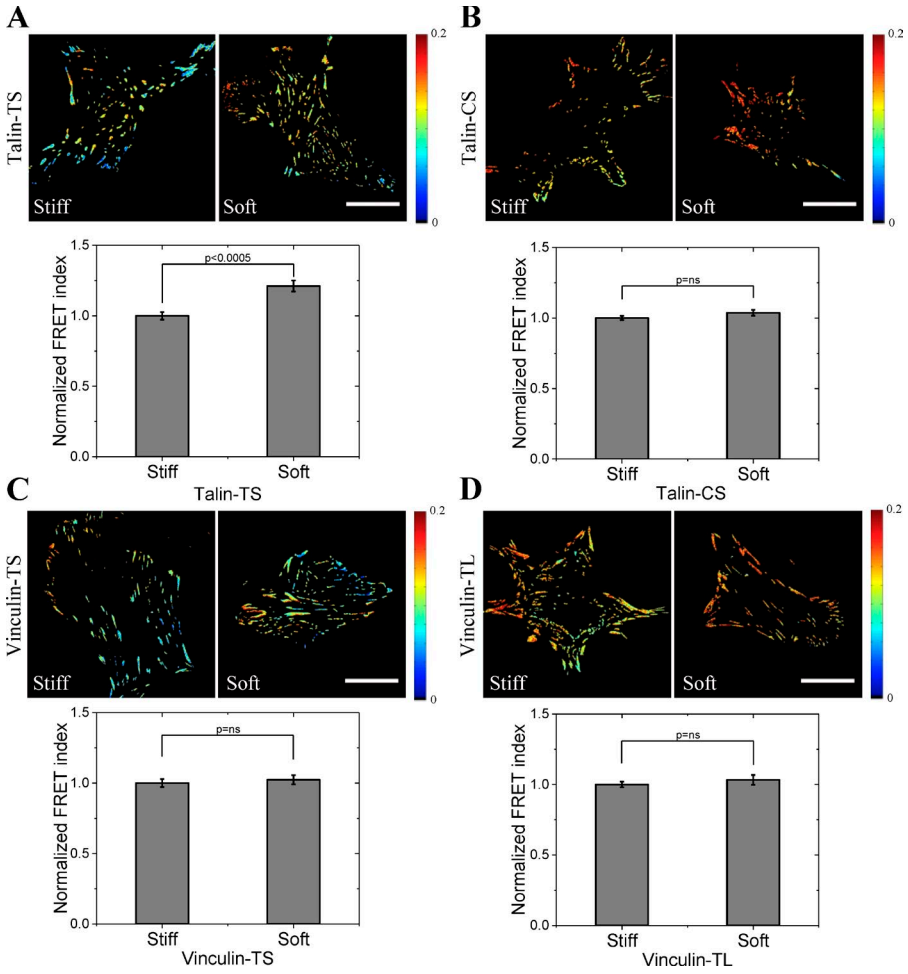

Figure 4. **Differential substrate stiffness sensing by talin and vinculin.** (A) Representative FRET map and normalized FRET index of talin-TS in talin1$^{-/-}$ cells on stiff (~30 kPa; n = 29) or soft (~3 kPa; n = 30) substrates. (B) Talin-CS on stiff (n = 27) or soft (n = 26) substrates. (C) Vinculin-TS expressed in vinculin$^{-/-}$ cells on stiff (n = 50) or soft (n = 45) substrates. (D) Vinculin–tailless control (vinculin-TL; control for zero tension) on stiff (n = 25) or soft (n = 25) substrates. Bars, 20 µm. Error bars represent SEM.

(K922E, Q923E, R1510E, and K1522E) only moderately reduced talin association with F-actin in sedimentation assays (Fig. S5 M). We therefore mutated two additional residues at the talin–actin interface (Fig. S5 M). Talin (K922E, Q923E, Q930E, K1500E, R1510E, and K1522E) showed an ~60% decrease in F-actin binding compared with wild type (Fig. S5 M). When these mutations were introduced into talin-TS, this construct localized to FAs (Fig. S5 N); however, force on talin in FAs was substantially reduced (Fig. 5, D and E). Cell area and phospho–myosin regulatory light chain levels were similar in talin-TS, ABS3, and ABS3 mutant talin-TS–transfected talin1$^{-/-}$ cells (Fig. S5, O–Q). To confirm these results, we also examined FRET efficiency by frequency domain lifetime imaging. This method showed very similar results (Fig. 5 F). In contrast to ABS3 mutant talin-TS, mutation in ABS2 also decreased total cell traction (Fig. S5, R and S). We conclude that ABS2 is the major ABS for force transmission in FAs in these cells.

Role of vinculin and ABSs in spatial regulation of tension and ECM rigidity sensing

We next addressed which interactions are critical for spatial regulation of talin tension. siRNA-mediated depletion of vinculin (and in vinculin$^{-/-}$ cells) had little effect on the difference between peripheral and central FAs (Fig. 6 A and Fig. S5 T). Thus, vinculin is not required for spatial differences. We then examined the roles of ABS2 and ABS3. Talin-TS with mutated ABS3 showed a marked reduction in the difference in tension between central and peripheral FAs (Fig. 6 B). In contrast, mutation of ABS2, despite the overall reduction in tension, preserved the difference between central and peripheral (Fig. 6 C).

We also examined the roles of vinculin, ABS2, and ABS3 in stiffness sensing. In vinculin$^{-/-}$ cells, despite the lower overall tension, tension across talin-TS was still lower on soft substrates (Fig. 6 D). Mutation of ABS2 abolished stiffness sensing without significantly changing the cell spreading area, whereas mutation of ABS3 had no effect (Fig. 6, E and F; and Fig. S5 U). Together, these data show that vinculin association with talin is required neither for differential tension in central versus peripheral FAs nor on soft versus stiff substrates; ABS2, but not ABS3, is required for stiffness sensing; ABS3, but not ABS2, is required for differential force on central versus peripheral adhesions.

Discussion

These studies report the development and validation of a talin-TS based on the nanospring derived from spider silk flagelliform. We found that FRET is decreased in talin-TS within FAs, whereas the talin-CS control shows high FRET under all conditions; this finding was validated by intensity FRET measurements (Fig. 2, A and B), acceptor photobleaching (Fig. S2, K and L), time domain FLIM (Fig. 2 H and Fig. S2 M), and frequency domain FLIM (Fig. 5 F). However, talin-TS and talin-CS show identical FRET efficiency in solution (Fig. 2 E),

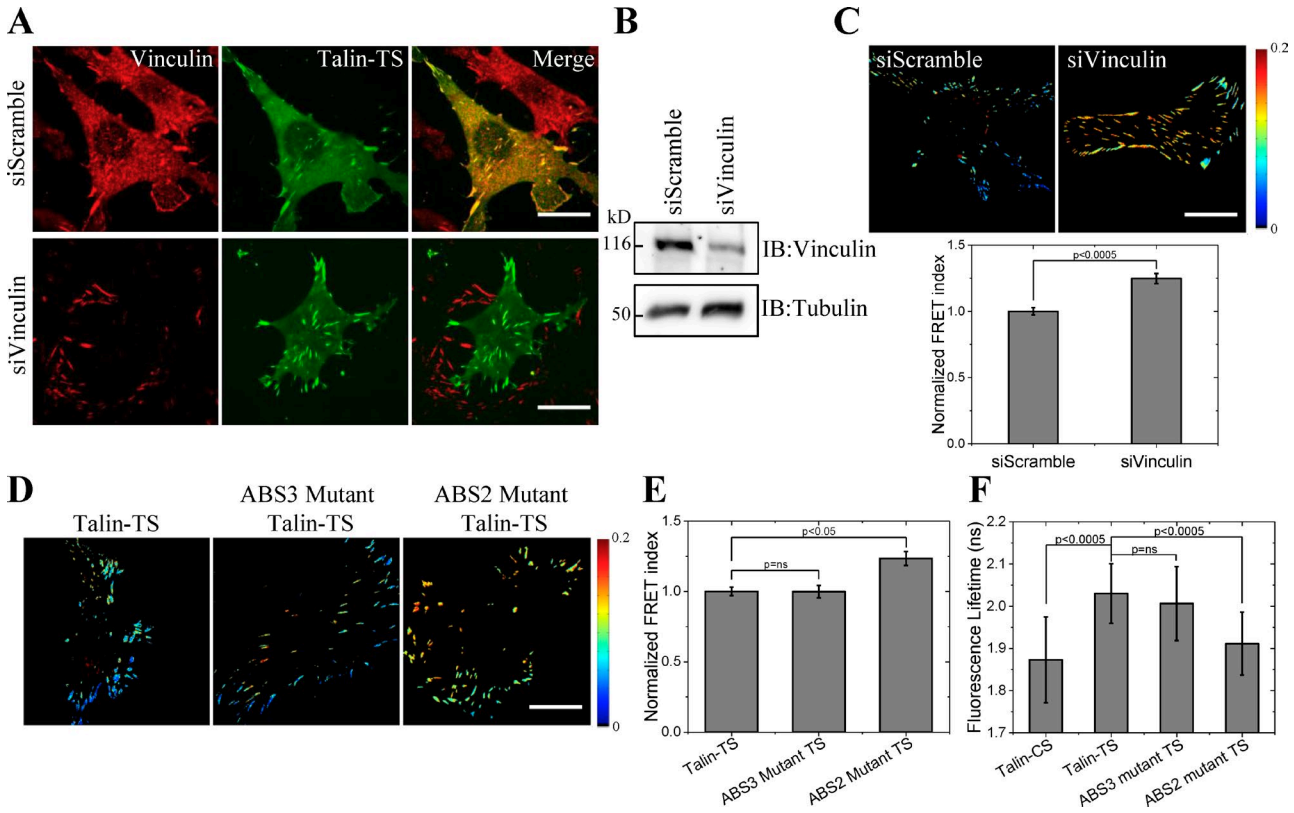

Figure 5. **Role of vinculin and ABS in regulating force on talin.** (A) Immunostaining of vinculin (red) in talin1$^{-/-}$ cells transfected with scrambled or vinculin siRNA. The talin-TS is in green. (B) Western blot for vinculin after knockdown. IB, immunoblot. (C) Representative FRET map and normalized FRET index of talin-TS in scrambled (n = 30) and vinculin (n = 32) siRNA–treated cells. (D and E) Representative FRET map (D) and normalized FRET index (E) of talin-TS (n = 46) or ABS3 mutant talin-TS (n = 37) and ABS2 mutant talin-TS (n = 31) transfected in talin1$^{-/-}$ cells. (F) Frequency domain EGFP lifetime for talin-CS (n = 74), talin-TS (n = 67), ABS3 mutant talin-TS (n = 66), and ABS2 mutant talin-TS (n = 66). Bars, 20 µm. Error bars represent SEM.

in the cytoplasm (Fig. 2, C and D), or membrane associated above the substrate (Fig. S2, A and B). Tension on talin-TS was reduced by inhibiting myosin (Fig. 2, F and G; and Fig. S2 E), increased by activating myosin II with LPA (Fig. S2, G and H), and lowered outside FAs (Fig. S2 R), whereas the talin-CS was again unaffected in all cases (Fig. S2, F and R). Together, these data strongly support the validity of talin-TS to report tension across this protein.

Current models for talin place the main integrin-binding site in the talin head domain and the main actin interaction sites in the rod domain (Puklin-Faucher and Sheetz, 2009; Wehrle-Haller, 2012; Goult et al., 2013). The sensor module located in between the head and rod domains should therefore specifically report the tension between the integrin and F-actin. This sensor would not report on internal forces within the individual domains. For example, if F-actin bound to ABS1, the sensor would be insensitive to forces between the integrin and ABS1; the sensor would similarly be insensitive to forces between ABS2 and ABS3 within the rod domain. This specificity may be useful for elucidating complex mechanical interactions in multidomain proteins. For talin, however, current views argue that the talin-TS reports on the major tension across the molecule.

These measurements show, first, that talin in FAs is under tension, with talin in peripheral FAs under higher tension than talin in central FAs that have characteristics of fibrillar adhesions. This result is somewhat surprising considering that tension is thought to be critical for adhesion formation and stability, with tension across talin as a major factor. Yet, the stability of central FA–fibrillar adhesions is comparable with peripheral FAs. These results suggest that central adhesions are stabilized by a mechanism that is distinct from peripheral FAs. It is also notable that tension on vinculin shows no such spatial variation. Vinculin staining relative to talin was very slightly higher in the periphery compared with the central region. Although we cannot completely exclude some effect of antibody accessibility in these differently structured adhesions, the crucial point to our minds is that the difference between central and peripheral adhesions persisted after vinculin deletion or depletion, and thus, differential vinculin binding cannot explain the spatial differences in talin tension. This result raises the possibility that vinculin in central adhesions is not linked to talin but through other interactions that could mediate force transmission (Turner et al., 1990; Bois et al., 2006). Our data also show that ABS3 but not ABS2 is required for the central–peripheral difference. Together, these data suggest that central adhesions are organized and regulated in a distinct manner from peripheral adhesions.

The maximal tension detected by the 40-aa spring used in the talin-TS is ~6 pN; above that, FRET efficiency goes to zero (Grashoff et al., 2010). Interestingly, even in peripheral FAs under the highest tension, the imaging modalities used in this study detected only a few pixels with zero FRET. With intensity or photobleaching methods, this result could be caused by averaging of talin molecules under high and low tension within each pixel. However, FLIM measurements failed to detect multiple components in the decay curves. Thus, talin is under moderate and relatively uniform tension, at least within the resolution of the sensor.

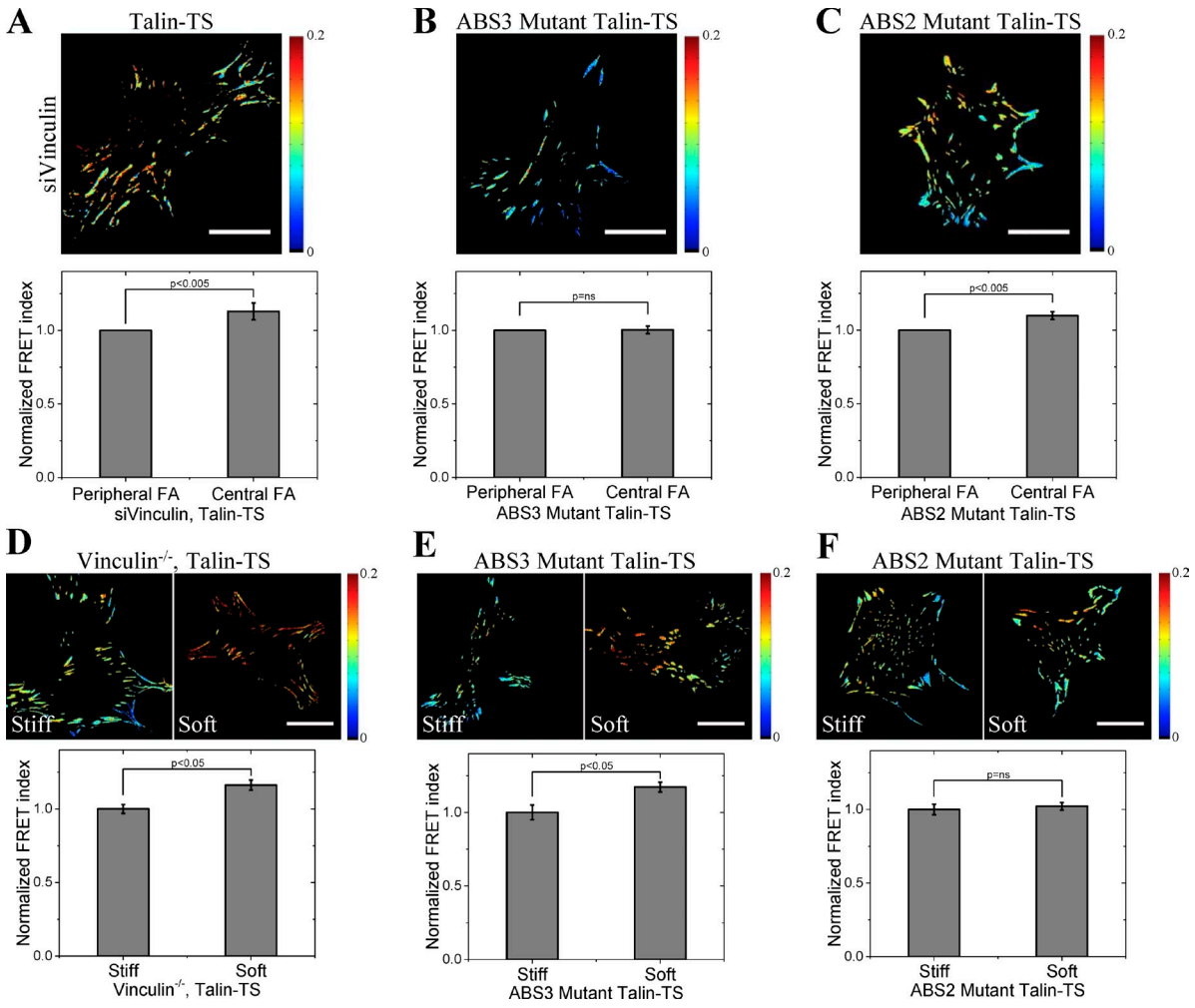

Figure 6. **Role of vinculin and ABSs in spatial variation and ECM stiffness sensing by talin.** (A–C) Representative FRET map and normalized FRET index of talin-TS in vinculin–knocked down talin1$^{-/-}$ cells (n = 29; A), ABS3 mutant talin-TS in talin1$^{-/-}$ cells (n = 18; B), and ABS2 mutant talin-TS in talin1$^{-/-}$ cells (n = 28; C) for central and peripheral FAs. (D–F) Representative FRET map and normalized FRET index of talin-TS in vinculin$^{-/-}$ cells plated on stiff (n = 30) and soft (n = 25) substrates (D), ABS3 mutant talin-TS in talin1$^{-/-}$ cells plated on stiff (n = 25) and soft (n = 25) substrates (E), and ABS2 mutant talin-TS in talin1$^{-/-}$ cells plated on stiff (n = 25) and soft (n = 25) substrates (F). Bars, 20 µm. Error bars represent SEM.

While this manuscript was in revision, Austen et al. (2015) described an alternative talin-TS based on folded peptide hairpins that denature at forces in the 7–11-pN range. Most of their results are consistent with ours; however, they found that a significant fraction of their 11-pN sensor was open in FAs, suggesting higher force. Any differences in reported tension across talin could be caused by some combination of differences in the way the in vitro calibrations are extrapolated to in vivo measurements or to differences in cell types and conditions.

Our results are interesting in light of available data on the FA clutch that transmits force between moving actin filaments and immobile, matrix-bound integrins (Case and Waterman, 2015). Speckle imaging of talin in FAs showed that talin moved rearward at about half of the speed of actin (Hu et al., 2007). This result implies that bonds between talin and integrin, and talin and actin, must rapidly form, break, and reform. Such fast kinetics are more consistent with some of these interactions behaving as "slip bonds" whose lifetime decreases as tension increases. Yet, FAs as a whole generally behave as "catch bonds" that strengthen under tension. This apparent paradox may be resolved by considering first that catch bonds only show this behavior within a certain range, with higher forces typically shortening bond lifetime (Hoffman et al., 2011). Second, the opening of talin helix bundles to allow binding of vinculin is a key component of FA force-dependent strengthening (Roca-Cusachs et al., 2012). Indeed, we found that deletion or depletion of vinculin reduced the force on talin. We therefore hypothesize that individual talin–actin and vinculin–actin bonds are slip bonds. Increasing the number of actin links by recruiting vinculin to talin stabilizes the associations, but they remain force sensitive to allow actin filaments to continue their rearward movement. In this model, catch bond behavior of FAs is an emergent property. However, talin–integrin bonds may be either catch bonds or else the affinity may be sufficiently high (~100 nM; Calderwood et al., 2002) to withstand substantial forces.

Our data also demonstrate that under the conditions studied, ABS2 rather than ABS3 is the critical load-bearing ABS. This finding was unexpected, as ABS3 has generally been thought to play the critical role, albeit without strong supporting data. However, the importance of ABS2 is also supported by

functional data published while this manuscript was in revision (Atherton et al., 2015), using the ABS2 mutant that we developed. These results do not exclude a role for ABS3 in other settings; indeed, ABS3 was required for differential tension in central versus peripheral talin. This result suggests that ABS3 may play a transient role in bearing force that is not readily detectable in steady-state measurements. Studies in flies also found that integrin–talin–actin linkages can be arranged in different ways in different tissues (Franco-Cea et al., 2010; Klapholz et al., 2015). Analysis of different cell types in different organisms will be an interesting direction for future work.

The finding that talin is under lower tension when cells are plated on soft substrata supports the general idea that talin tension is variable under different conditions. Interestingly, this behavior does not require vinculin. Together, these results have important implications for molecular mechanisms of stiffness sensing. It is now thought that stiffness sensing is mediated by a kinetic mechanism in which loading rate on the integrin–actin linkage varies (Chan and Odde, 2008; Hoffman et al., 2011; Plotnikov et al., 2012). In brief, cells exert traction forces on the substrate, which increase tension across this linkage; however, on soft substrates, movement of the substrate reduces the loading rate so that force builds up more slowly. High loading rates on stiff surfaces activate catch bonds more effectively, leading to FA strengthening. Unfolding of talin rod domain helical bundles to promote vinculin binding is thought to be an important aspect of this mechanism. However, the finding that force across talin is modulated by surface stiffness in the absence of vinculin argues that vinculin-dependent reinforcement is a downstream consequence of prior events. What could these events be? Integrins themselves show catch bond behavior on a time scale of seconds (Kong et al., 2009), which is distinctly faster than vinculin recruitment and thus is not likely vinculin dependent. Together, these results lead us to propose that stiffness sensing involves stabilization of the integrin–talin association. This could occur through a conformational transition in the integrin or in the talin head domain or both. Sustained force on talin could then promote helix unfolding and vinculin binding to provide additional reinforcement.

In summary, development of a talin-TS has produced results that significantly alter our understanding of how the integrin–talin–actin linkage functions in the FA clutch. Further work will require combining talin tension measurements with single molecule imaging methods and genetic tools to test the hypotheses proposed here and to understand mechanisms of stiffness sensing and mechanotransduction in greater detail.

Materials and methods

Cell culture and transfection

Talin1$^{-/-}$ cell lines (Priddle et al., 1998) were cultured in DMEM/F12 (Gibco) with 10% FBS (Gibco), penicillin-streptomycin (Gibco), β-mercaptoethanol (5 µl in 500 ml; Sigma-Aldrich), and sodium bicarbonate (8 ml of 7.5% [wt/vol] in 500 ml media; Sigma-Aldrich). NIH 3T3 (ATCC) and vinculin$^{-/-}$ cells, obtained from vinculin-null embryonic day 10.5 mice (Coll et al., 1995; Xu et al., 1998), were cultured in DMEM (Gibco) with 10% FBS and penicillin-streptomycin. Talin1$^{-/-}$ and vinculin$^{-/-}$ cells were provided by D. Critchley (University of Leicester, Leicester, England, UK) and E. Adamson (Sanford-Burnham Research Institute, La Jolla, CA), respectively. Cells were plated in antibiotic-free media 1 d before transfections. Talin1$^{-/-}$ cells were transfected using Jetprime reagent (Polyplus) according to the manufacturer's protocol. 3T3 and vinculin$^{-/-}$ cells were transfected using Lipofectamine 2000 (Invitrogen). Paxillin-EGFP was a gift from R. Horwitz (University of Virginia, Charlottesville, VA). Unless otherwise noted, cells were plated for 3 h in glass-bottom (MatTek Corporation) dishes coated with 10 µg/ml fibronectin overnight at 4°C and then imaged. Endogenous integrin β3 was blocked by adding cyclo (Arg-Gly-Asp-D-Phe-Val; cyclo RGD; 4304-v; Peptides International) to suspended cells with media for 5 min before plating. Blebbistatin (B0560; Sigma-Aldrich) and LPA (sc-201053; Santa Cruz Biotechnology, Inc.) were added to cells plated on dishes.

Construction of TS plasmids

The TS module EGFP-F40-tagRFP was first assembled into the vector pBluescript II(-)(ΔSalI, ΔNotI) by using the restriction sites XhoI–ApaI–NdeI–NotI. F40 refers to the 40-aa peptide $(GPGGA)_8$ derived from the elastic spider silk protein flagelliform. In the pBluescript II(-)(ΔSalI, ΔNotI) vector, the TS module was ligated into mouse talin1 fragment (1–3,217 bp) immediately after amino acid 447, where a SalI–NotI linker had been introduced. To complete the assembly of the talin-TS, the talin fragment-TS module was cut out with EcoRI–XhoI sites by using one XhoI site within Talin1 at 3,212 bp and ligated to talin rod fragments (3,212–7,623 bp) using EcoRI–XhoI sites in the mammalian expression vector pLPCX(ΔXhoI), which contains talin rod fragments (2,445–7,623 bp) between NotI and ClaI sites. To construct the talin C-terminal CS, the TS module with a 15-aa linker (GST SGSGKPGSGEGS) at its N terminus was assembled between ClaI and NotI sites after talin1 using the PCR-based Gibson assembly method. To construct the vinculin TS with the EGFP/tagRFP FRET pair, the module was inserted into vinculin after its head domain (amino acids 1–851), where a SalI–NotI linker had been introduced in pBluescript II(-)(ΔSalI, ΔNotI). The entire vinculin-TS module fragment was digested out and ligated into mammalian expression vector pcDNA3.1(+) using HindIII–EcoRI sites.

Knockdown and Western blot

Talin2 knockdown used 100 nM mouse Tln2 (70549; ON-TARGETplus; SMARTpool) siRNA (Tln2#1, 5′-GAGGGAAGAUGAGGGCUAA-3′; Tln2#2, 5′-GAACGUUUGUUGACUACCA-3′; Tln2#3, 5′-UGGCAGGGAUUUCACAGAA-3′; Tln2#4, 5′-CGAAUGAGCCUGUGAGCGA-3′; GE Healthcare), and scrambled control siRNA (AM4636; Ambion) using RNAimax (Invitrogen). Cells were transfected twice, the first time after freshly plating overnight and again 72 h later to obtain more efficient depletion. Two vinculin siRNA sequences (Vin#1, 5′-GGAAGAAAUCACAGAAUCAUU-3′; Vin#2, 5′-CCAGAUGAGUAAAGGAGUAUU-3′) were custom made (GE Healthcare). These two were mixed and used at 100 nM with double transfections, as described in the Cell culture and transfection section. Knockdown efficiency was confirmed by Western blotting of cell lysates in radioimmunoprecipitation assay (RIPA) buffer (25 mM Tris-HCl, pH 7.5 [Sigma-Aldrich], 150 mM NaCl [JT Baker], 1% NP-40 [Sigma-Aldrich], 1% sodium deoxycholate [Sigma-Aldrich], and 0.1% SDS [American Bioanalytical] in milliQ water); protease and phosphatase inhibitor (Thermo Fisher Scientific) was added just before extraction. After 2 h of transfection, cells were treated with calpain inhibitor cocktail (20 µM each of ALLN, calpain inhibitor III, and calpeptin; EMD Millipore) for 24 h and then were lysed in RIPA buffer. To separate the FA-associated insoluble talin sensor from the soluble pool, sensor-transfected cells were plated overnight on a 10 µg/ml fibronectin–coated dish. Soluble lysate was collected by washing cells in cold PBS and then adding buffer (Plopper and Ingber, 1993) containing 0.5% Triton X-100 (American Bioanalytical), 50 mM NaCl, 300 mM

sucrose (Sigma-Aldrich), 3 mM $MgCl_2$ (EMD Millipore), and 10 mM Pipes (Acros Organics), pH 6.8, with 1× protease and phosphatase inhibitor to cells on ice for 1.5 min. Next, FA-associated insoluble protein lysates were collected by adding RIPA buffer. Protein was resolved using SDS-PAGE and transferred to the nitrocellulose membrane using a transfer system (Trans-Blot Turbo; Bio-Rad Laboratories). The membrane was blocked using 5% skimmed milk (American Bioanalytical) in TBS with 0.1% Tween 20 (TBST; Sigma-Aldrich) and incubated with the following primary antibodies diluted in TBST overnight at 4°C: rabbit GFP (1:2,000; A111-22; Invitrogen), mouse talin1 (1:2,000; clone 93E12; ab104913; Abcam), mouse talin2 (1:2,000; clone 6E7; AC14-0126; Abcore), rabbit phospho–myosin light chain 2 (1:2,000; ser19; #3671; Cell Signaling Technology), mouse vinculin (1:2,000; V9131; Sigma-Aldrich), goat anti-actin (1:2,000; C-11; sc-1615; Santa Cruz Biotechnology, Inc.), and mouse tubulin (1:2,000; clone DM1a; Sigma-Aldrich). The membrane was washed with TBST for 5 min 3× at RT on a shaker. The membrane was then incubated with the appropriate HRP-conjugated secondary antibody (Santa Cruz Biotechnology, Inc.) diluted in TBST (1:5,000) and visualized using chemiluminescence detection method with Supersignal West Pico (Thermo Fisher Scientific) on the G:Box system (Syngene).

Immunostaining and antibodies

Cells were fixed in 4% paraformaldehyde in PBS for 20 min and permeabilized with 0.1% Triton X-100 in PBS for 20 min at RT. Cells were blocked with 1% BSA in PBS for 1 h at RT and then incubated with primary antibody at 4°C overnight. The following primary antibodies were used with the given dilution in 1% BSA in PBS: mouse paxillin (1:200; clone 349; BD), mouse vinculin (1:500), Armenian hamster integrin β1 (1:200; clone HMb1-1; cd29; BioLegend), mouse zyxin (1:1,000; Sigma-Aldrich), rabbit phospho-paxillin Y31 (1:400; 44-720G; Invitrogen), rabbit phospho-paxillin Y118 (1:400; 44-722G; Invitrogen), rabbit fibronectin (1:1,000; F3648; Sigma-Aldrich), rabbit tensin1 (1:300; SAB4200283; Sigma-Aldrich), rabbit phospho-myosin (1:100), and rabbit integrin β3 (1:100; ab75872; Abcam). Cells were washed in PBS thrice and then incubated with Alexa Fluor 647–conjugated secondary antibody diluted in PBS (1:1,000; Invitrogen) at RT for 1 h. Actin was labeled using Alexa Flour 488–, 647–, and 568–conjugated phalloidin (1:200; Molecular Probes).

FRAP

FRAP experiments were performed on a microscope (Eclipse Ti; Nikon) equipped with a spinning disk confocal imaging system (Ultraview Vox; PerkinElmer) and an electron-multiplying charged-coupled device camera (C9100-50; Hamamatsu Photonics), using a 100×, 1.4 NA oil objective. Cells were maintained at 37°C with humidity and CO_2 control. Images were acquired using Velocity 6.6.1 software. Three prebleach images at 2-s intervals and then a laser pulse at 100% power of the 488-nm line were used to bleach a circular region of 2-µm diameter. Time-lapse images were then acquired every 10 s for 4 min. Images were corrected for photobleaching during image acquisition, and normalized FRAP curves were plotted.

FRET imaging and analysis

These analyses were done essentially as previously described (Grashoff et al., 2010). High resolution live FRET imaging was performed on an Eclipse Ti microscope equipped with an Ultraview Vox spinning disk confocal imaging system and an electron-multiplying charged-coupled device C9100-50 camera, using a 100×, 1.4 NA oil objective at 37°C with humidity and CO_2 control. Images were acquired using Velocity software. Three sequential images with 500-ms exposure times were acquired with the following filter combinations: donor (EGFP) channel with a 488-nm line (ex) and 527/55 (em), acceptor (or tagRFP) channel with a 561-nm line (ex) and 615/70 (em), and FRET channel with a 488-nm line (ex) and 615/70 (em). Donor leakage was determined from EGFP-transfected cells, whereas acceptor cross excitation was obtained from tagRFP-transfected cells. For all the calculations, respective background subtraction, illumination gradient, and pixel shift correction were performed followed by three-point smoothening. The slope of pixel-wise donor or acceptor channel intensity versus FRET channel intensity gives leakage (x) or cross-excitation (y) fraction, respectively. FRET map and pixel-wise FRET index for the sensors were determined from

$$FRET\ index = \frac{FRET\ channel - x\,(Donor\ channel) - y(Acceptor\ channel)}{Acceptor\ channel}.$$

FAs were thresholded using intensity and size cutoff criteria. Regions within the adhesions were used to obtain mean FRET index per cell. Student's *t* test was performed between the two groups to calculate statistical significance and p-value. At least $P < 0.05$ was considered significant. For central versus peripheral FA FRET histograms, paired Student's *t* test was performed. Other confocal images were acquired also on the same microscope using 100×, 1.4 NA oil or 60×, 1.4 NA oil or 20×, 0.45 NA air objective at 37°C with humidity and CO_2 control for live cell images or at RT for fixed cells. For live cell imaging, phenol red minus fluorobrite DMEM (Gibco) with 10% FBS (Gibco) and penicillin-streptomycin media were used, whereas normal culture media was used for the rest of the live cell imaging. ImageJ (National Institutes of Health) was used for basic image processing. All analyses were done using custom-written software (MATLABR2014a; MathWorks). Graphs were plotted in Origin (9.1; 64 bit).

FRET in cell lysates

293T cells transfected with EGFP (donor leakage control), tagRFP (acceptor cross-excitation control), talin-CS, and talin-TS (and untransfected cells for background) were lysed in 50 mM Hepes (Sigma-Aldrich), 50 mM NaCl, 5 mM EDTA (JT Baker), 1% Triton X-100, 50 mM NaF (Sigma-Aldrich), and 10 mM sodium pyrophosphate tetrabasic (Sigma-Aldrich), pH 7.4, with protease and phosphatase inhibitor (Thermo Fisher Scientific); sonicated; and spun at 10,000 rpm at 4°C for 15 min for clarification. 200 µl of lysates was used for fluorescence reading in 96-well plate using a spectrophotometer (Synergy-HT; Bio-tek). Three readings per well were performed using the following excitation and emission filter combinations: donor (EGFP) channel with 485/20 (ex) and 530/25 (em), acceptor (or tagRFP) channel with 545/40 (ex) and 620/40 (em), and FRET channel with 485/20 (ex) and 620/40 (em). FRET index was determined by the equation in the FRET imaging and analysis section.

FRET by acceptor photobleaching

Acceptor photobleaching was performed on the Eclipse Ti microscope using a 100×, 1.4 NA oil objective. EGFP was excited using a 488-nm line of an argon ion laser and collected using 527/55 filter, whereas for tagRFP, a 561-nm laser line was used and collected using 615/70 filter. The acceptor was bleached using a 561-nm laser. FRET was calculated by taking the ratio of donor intensity images before and after bleaching the acceptor: $\left(\eta = 1 - I_{donor\ pre\ bleach}/I_{donor\ post\ bleach}\right)$.

Time-correlated single photon counting (TCSPC) FLIM-FRET acquisition and analysis

TCSPC FLIM images were acquired on a multiphoton microscope (Trim-scope 2; LaVision Biotec) using a 100×, 1.4 NA objective

(Nikon). The excitation source was a system (Ultra 2 ti:sapphire; Coherent Chameleon) outputting a wavelength of 890 nm. All acquisition times were of the order of 20 s. The detector used was a cooled hybrid photomultiplier tube (Hamamatsu Photonics) in TCSPC mode. During imaging, cells were sealed using parafilm and kept at 37°C using a stage heater. Laser power levels were kept low enough to avoid saturated pixels within the image.

For the analysis, the files were exported from InSpectorPro 5 as OME-Tiffs and imported into the FLIMfit software tool developed at Imperial College London.

To fit the data, a biexponential model was used for all datasets, and the weighted mean lifetime was used for comparison. The global fitting method was used in which the two lifetimes are kept constant across the members of a particular dataset and the fractional contribution from each is allowed to vary between members of the same dataset, resulting in a spatially dependent weighted mean lifetime distribution.

Frequency domain FLIM–total internal reflectance was performed using a FLIM attachment system (Lambert Instruments), coupled to an inverted microscope (TE-2000E; Nikon) with Perfect Focus. Total internal reflectance microscopy was performed using a 100×, 1.45 NA objective (Plan Apo; Nikon) and custom-built condenser, which delivers light from a 488-nm laser (DeepStar; Omicron) through an optical fiber into a conjugate plane of the objective back focal plane. Data were acquired and analyzed using LiFLIM software version 1.1.11.

PDMS substrate preparation and traction force microscopy

A high resolution microscopy-compatible thin layer of PDMS substrate on glass-bottom dishes was fabricated by spin coating 300 µl silicone at 6,000 rpm. Approximately 3 kPa (Style et al., 2014) was made by thoroughly mixing silicone and curing agent (CY-52-276A and CY-52-276B; Dow Corning) at a 1:1 ratio. Spin-coated dishes were kept at RT overnight for curing. Approximately 30 kPa stiff substrates (Ochsner et al., 2007) was made from Sylgard 184 (Dow Corning) by mixing base and curing agent in a 40:1 ratio; spin-coated dishes were kept at 80°C for 3 h for curing. These dishes were then UV treated in a culture hood for 20 min before coating with fibronectin. 1 kPa substrate (Gutierrez and Groisman, 2011) was prepared by mixing the A and B components of the silicone gel at a ratio of 1.2:1, whereas 1.3 MPa (Ochsner et al., 2007) substrates from Sylgard 184 was prepared by mixing base and curing agent in a 10:1 ratio. To carry out traction force microscopy (Mertz et al., 2013; Style et al., 2014), spin-coated thin ∼3-kPa PDMS–layered glass substrate was prepared as described above. However, this PDMS layer was sandwiched between two layers of fluorescent beads: a bottom layer (F8797; Thermo Fisher Scientific) on glass that serves as fiduciary markers to determine the PDMS thickness, and a top layer (F8807; Thermo Fisher Scientific) on PDMS that serves as the markers to track displacement caused by cell traction. Top bead images with and without cells (removed by adding 0.1% SDS in PBS) were acquired, and traction force measurement and total work done was calculated using custom-written MATLAB code (Mertz et al., 2012, 2013) from E. Dufresne's laboratory. We thank E. Dufresne and R. Boltyanskiy (Yale University, New Haven, CT) for their instruction and assistance with this procedure.

Validation of mutants that disrupt ABS2 in the talin rod

Sequence conservation of talin 913–1044 and 1461–1580. The sequences of talin residues 913–1944 (R4) and 1461–1580 (R8) were aligned across species. The alignment was performed using T-Coffee (Notredame et al., 2000) using the following sequences: *Mus musculus* talin-1, *M. musculus* talin-2, *Homo sapiens*, *Gallus gallus*, *Danio rerio*, *Drosophila melanogaster*, and *Caenorhabditis elegans*. The map of surface-exposed conserved residues is shown in Fig. S5 L (invariant, red; conserved, yellow).

R4 and R8 have anomalously high pI values of 9.5 and 7.8, compared with the mean pI of 5.4 of the talin rod. At physiological pH, these domains will be positively charged, as expected for the interaction with the negatively charged surface of actin filaments. These characteristics are similar to ABS3 (Gingras et al., 2008), making the conserved patches of R4 and R8 the regions that likely interact with F-actin. The conserved basic surfaces on R4 and R8 were mutated as follows: 4× for K922E/Q923E/R1510E/K1522E and 6× for K922E/Q923E/Q930E/K1500E/R1510E/K1522E.

Protein expression and purification. Talin constructs were synthesized by PCR, using a mouse talin1 cDNA as a template, and cloned into pET-151/D-TOPO (Invitrogen). Constructs were expressed in *Escherichia coli* (DE3; BL21 Star; Thermo Fisher Scientific) cultured in lysogeny broth (LB). Recombinant His-tagged talin polypeptides were purified as described previously (Goult et al., 2009). Protein concentrations were determined using the respective extinction coefficients at 280 nm based on absorption coefficients calculated from the aromatic content according to ProtParam.

Actin cosedimentation assays. Rabbit skeletal muscle G-actin (Pardee and Spudich, 1982) was polymerized in 10 mM Tris, 50 mM NaCl, 100 µM ATP, 1 mM DTT, and 1 mM $MgCl_2$, pH 7.0. Assays were performed using 4 µM talin polypeptides and 10 µM F-actin. The mixture was incubated for 60 min at RT and centrifuged at 50,000 rpm for 30 min at 22°C using an ultracentrifuge (Optima TM; Beckman Coulter). Supernatants and pellets were analyzed on 12% SDS-PAGE gels and stained using Coomassie blue.

Online supplemental material

Fig. S1 shows additional characterization of the talin sensor and talin1$^{-/-}$ cell line. Fig. S2 contains additional controls for talin-TS. It also shows characterization of peripheral and central FAs in terms of talin tension. Fig. S3 shows the compositional difference in central and peripheral FAs. Fig. S4 shows the differential amount of integrin β3 in central and peripheral FAs and its correlation with FRET in talin-TS. Correlation between amount of integrin β1 in FAs and substrate stiffness is also shown. Fig. S5 shows effect of substrate stiffness on tension in vinculin. It also contains characterization of ABS2 mutant talin and various comparisons between talin-TS, ABS3 mutant talin-TS, and ABS2 mutant talin-TS. Online supplemental material has MATLAB code, included in a zip file, used to calculate FRET index from raw intensity images. The code also generates the FRET index map and the pixel-wise histogram of FRET indices, as well as mean FRET index per cell. Any channel intensity corresponding to pixels, where FRET is calculated, can also be obtained using this code. Online supplemental material is available at http://www.jcb.org/cgi/content/full/jcb.201510012/DC1.

Acknowledgments

We thank Drs. Rostislav Boltyanskiy and Eric Dufresne for helping with the PDMS spin coating and sharing the traction force measurement software code. The EGFP-tagged paxillin plasmid was a kind gift from Dr. Alan R. Horwitz's laboratory. Talin1$^{-/-}$ and Vinculin$^{-/-}$ cells were kind gifts from Dr. David R. Critchley and Dr. Eileen D. Adamson, respectively.

This work was supported by a U.S. Public Health Service grant (PO1 GM98412) to M.A. Schwartz. E.J. McGhee and K.I. Anderson were supported by Cancer Research UK with a core grant fund. K. Tanaka was supported by Japan Society for the Promotion of Science postdoctoral fellowships for abroad research.

The authors declare no competing financial interests.

Author contributions: A. Kumar and M.A. Schwartz designed the experiments. A. Kumar and K. Van den Dries carried out the experiments and analyzed the data. M.A. Schwartz, E.J. McGhee, and K.I. Anderson conducted the FLIM-FRET experiment and analyzed the data. M.D. Anderson and B.T. Goult carried out the characterization of the talin ABS2 mutant. M. Ouyang and K. Tanaka made the talin sensor and control plasmids, respectively. A. Groisman provided the PDMS substrate. A. Kumar and M.A. Schwartz wrote the paper.

Submitted: 3 October 2015
Accepted: 5 April 2016

References

Atherton, P., B. Stutchbury, D.Y. Wang, D. Jethwa, R. Tsang, E. Meiler-Rodriguez, P. Wang, N. Bate, R. Zent, I.L. Barsukov, et al. 2015. Vinculin controls talin engagement with the actomyosin machinery. *Nat. Commun.* 6:10038. http://dx.doi.org/10.1038/ncomms10038

Austen, K., P. Ringer, A. Mehlich, A. Chrostek-Grashoff, C. Kluger, C. Klingner, B. Sabass, R. Zent, M. Rief, and C. Grashoff. 2015. Extracellular rigidity sensing by talin isoform-specific mechanical linkages. *Nat. Cell Biol.* 17:1597–1606. http://dx.doi.org/10.1038/ncb3268

Balaban, N.Q., U.S. Schwarz, D. Riveline, P. Goichberg, G. Tzur, I. Sabanay, D. Mahalu, S. Safran, A. Bershadsky, L. Addadi, and B. Geiger. 2001. Force and focal adhesion assembly: a close relationship studied using elastic micropatterned substrates. *Nat. Cell Biol.* 3:466–472. http://dx.doi.org/10.1038/35074532

Beckerle, M.C., K. Burridge, G.N. DeMartino, and D.E. Croall. 1987. Colocalization of calcium-dependent protease II and one of its substrates at sites of cell adhesion. *Cell.* 51:569–577. http://dx.doi.org/10.1016/0092-8674(87)90126-7

Beningo, K.A., M. Dembo, I. Kaverina, J.V. Small, and Y.L. Wang. 2001. Nascent focal adhesions are responsible for the generation of strong propulsive forces in migrating fibroblasts. *J. Cell Biol.* 153:881–888. http://dx.doi.org/10.1083/jcb.153.4.881

Bois, P.R., B.P. O'Hara, D. Nietlispach, J. Kirkpatrick, and T. Izard. 2006. The vinculin binding sites of talin and α-actinin are sufficient to activate vinculin. *J. Biol. Chem.* 281:7228–7236. http://dx.doi.org/10.1074/jbc.M510397200

Brown, N.H., S.L. Gregory, W.L. Rickoll, L.I. Fessler, M. Prout, R.A. White, and J.W. Fristrom. 2002. Talin is essential for integrin function in *Drosophila*. *Dev. Cell.* 3:569–579. http://dx.doi.org/10.1016/S1534-5807(02)00290-3

Butcher, D.T., T. Alliston, and V.M. Weaver. 2009. A tense situation: forcing tumour progression. *Nat. Rev. Cancer.* 9:108–122. http://dx.doi.org/10.1038/nrc2544

Calderwood, D.A., B. Yan, J.M. de Pereda, B.G. Alvarez, Y. Fujioka, R.C. Liddington, and M.H. Ginsberg. 2002. The phosphotyrosine binding-like domain of talin activates integrins. *J. Biol. Chem.* 277:21749–21758. http://dx.doi.org/10.1074/jbc.M111996200

Calderwood, D.A., I.D. Campbell, and D.R. Critchley. 2013. Talins and kindlins: partners in integrin-mediated adhesion. *Nat. Rev. Mol. Cell Biol.* 14:503–517. http://dx.doi.org/10.1038/nrm3624

Case, L.B., and C.M. Waterman. 2015. Integration of actin dynamics and cell adhesion by a three-dimensional, mechanosensitive molecular clutch. *Nat. Cell Biol.* 17:955–963. http://dx.doi.org/10.1038/ncb3191

Chan, C.E., and D.J. Odde. 2008. Traction dynamics of filopodia on compliant substrates. *Science.* 322:1687–1691. http://dx.doi.org/10.1126/science.1163595

Chrzanowska-Wodnicka, M., and K. Burridge. 1996. Rho-stimulated contractility drives the formation of stress fibers and focal adhesions. *J. Cell Biol.* 133:1403–1415. http://dx.doi.org/10.1083/jcb.133.6.1403

Coll, J.L., A. Ben-Ze'ev, R.M. Ezzell, J.L. Rodríguez Fernández, H. Baribault, R.G. Oshima, and E.D. Adamson. 1995. Targeted disruption of vinculin genes in F9 and embryonic stem cells changes cell morphology, adhesion, and locomotion. *Proc. Natl. Acad. Sci. USA.* 92:9161–9165. http://dx.doi.org/10.1073/pnas.92.20.9161

Costa, P., F.V. Almeida, and J.T. Connelly. 2012. Biophysical signals controlling cell fate decisions: how do stem cells really feel? *Int. J. Biochem. Cell Biol.* 44:2233–2237. http://dx.doi.org/10.1016/j.biocel.2012.09.003

Cram, E.J., S.G. Clark, and J.E. Schwarzbauer. 2003. Talin loss-of-function uncovers roles in cell contractility and migration in *C. elegans*. *J. Cell Sci.* 116:3871–3878. http://dx.doi.org/10.1242/jcs.00705

Franco-Cea, A., S.J. Ellis, M.J. Fairchild, L. Yuan, T.Y. Cheung, and G. Tanentzapf. 2010. Distinct developmental roles for direct and indirect talin-mediated linkage to actin. *Dev. Biol.* 345:64–77. http://dx.doi.org/10.1016/j.ydbio.2010.06.027

Gingras, A.R., N. Bate, B.T. Goult, L. Hazelwood, I. Canestrelli, J.G. Grossmann, H. Liu, N.S. Putz, G.C. Roberts, N. Volkmann, et al. 2008. The structure of the C-terminal actin-binding domain of talin. *EMBO J.* 27:458–469. http://dx.doi.org/10.1038/sj.emboj.7601965

Goult, B.T., N. Bate, N.J. Anthis, K.L. Wegener, A.R. Gingras, B. Patel, I.L. Barsukov, I.D. Campbell, G.C. Roberts, and D.R. Critchley. 2009. The structure of an interdomain complex that regulates talin activity. *J. Biol. Chem.* 284:15097–15106. http://dx.doi.org/10.1074/jbc.M900078200

Goult, B.T., T. Zacharchenko, N. Bate, R. Tsang, F. Hey, A.R. Gingras, P.R. Elliott, G.C. Roberts, C. Ballestrem, D.R. Critchley, and I.L. Barsukov. 2013. RIAM and vinculin binding to talin are mutually exclusive and regulate adhesion assembly and turnover. *J. Biol. Chem.* 288:8238–8249. http://dx.doi.org/10.1074/jbc.M112.438119

Grashoff, C., B.D. Hoffman, M.D. Brenner, R. Zhou, M. Parsons, M.T. Yang, M.A. McLean, S.G. Sligar, C.S. Chen, T. Ha, and M.A. Schwartz. 2010. Measuring mechanical tension across vinculin reveals regulation of focal adhesion dynamics. *Nature.* 466:263–266. http://dx.doi.org/10.1038/nature09198

Gutierrez, E., and A. Groisman. 2011. Measurements of elastic moduli of silicone gel substrates with a microfluidic device. *PLoS One.* 6:e25534. http://dx.doi.org/10.1371/journal.pone.0025534

Hirata, H., H. Tatsumi, and M. Sokabe. 2008. Mechanical forces facilitate actin polymerization at focal adhesions in a zyxin-dependent manner. *J. Cell Sci.* 121:2795–2804. http://dx.doi.org/10.1242/jcs.030320

Hoffman, B.D., C. Grashoff, and M.A. Schwartz. 2011. Dynamic molecular processes mediate cellular mechanotransduction. *Nature.* 475:316–323. http://dx.doi.org/10.1038/nature10316

Hotulainen, P., and P. Lappalainen. 2006. Stress fibers are generated by two distinct actin assembly mechanisms in motile cells. *J. Cell Biol.* 173:383–394. http://dx.doi.org/10.1083/jcb.200511093

Hu, K., L. Ji, K.T. Applegate, G. Danuser, and C.M. Waterman-Storer. 2007. Differential transmission of actin motion within focal adhesions. *Science.* 315:111–115. http://dx.doi.org/10.1126/science.1135085

Humphrey, J.D., E.R. Dufresne, and M.A. Schwartz. 2014. Mechanotransduction and extracellular matrix homeostasis. *Nat. Rev. Mol. Cell Biol.* 15:802–812. http://dx.doi.org/10.1038/nrm3896

Karpova, T.S., C.T. Baumann, L. He, X. Wu, A. Grammer, P. Lipsky, G.L. Hager, and J.G. McNally. 2003. Fluorescence resonance energy transfer from cyan to yellow fluorescent protein detected by acceptor photobleaching using confocal microscopy and a single laser. *J. Microsc.* 209:56–70. http://dx.doi.org/10.1046/j.1365-2818.2003.01100.x

Kim, D.H., S.B. Khatau, Y. Feng, S. Walcott, S.X. Sun, G.D. Longmore, and D. Wirtz. 2012. Actin cap associated focal adhesions and their distinct role in cellular mechanosensing. *Sci. Rep.* 2:555. http://dx.doi.org/10.1038/srep00555

Klapholz, B., S.L. Herbert, J. Wellmann, R. Johnson, M. Parsons, and N.H. Brown. 2015. Alternative mechanisms for talin to mediate integrin function. *Curr. Biol.* 25:847–857. http://dx.doi.org/10.1016/j.cub.2015.01.043

Kong, F., A.J. García, A.P. Mould, M.J. Humphries, and C. Zhu. 2009. Demonstration of catch bonds between an integrin and its ligand. *J. Cell Biol.* 185:1275–1284. http://dx.doi.org/10.1083/jcb.200810002

Kopp, P.M., N. Bate, T.M. Hansen, N.P. Brindle, U. Praekelt, E. Debrand, S. Coleman, D. Mazzeo, B.T. Goult, A.R. Gingras, et al. 2010. Studies on the morphology and spreading of human endothelial cells define key inter- and intramolecular interactions for talin1. *Eur. J. Cell Biol.* 89:661–673. http://dx.doi.org/10.1016/j.ejcb.2010.05.003

Lagarrigue, F., P. Vikas Anekal, H.S. Lee, A.I. Bachir, J.N. Ablack, A.F. Horwitz, and M.H. Ginsberg. 2015. A RIAM/lamellipodin-talin-integrin complex forms the tip of sticky fingers that guide cell migration. *Nat. Commun.* 6:8492. http://dx.doi.org/10.1038/ncomms9492

Lele, T.P., J. Pendse, S. Kumar, M. Salanga, J. Karavitis, and D.E. Ingber. 2006. Mechanical forces alter zyxin unbinding kinetics within focal adhesions of living cells. *J. Cell. Physiol.* 207:187–194. http://dx.doi.org/10.1002/jcp.20550

Li, Q., A. Kumar, E. Makhija, and G.V. Shivashankar. 2014. The regulation of dynamic mechanical coupling between actin cytoskeleton and nucleus by matrix geometry. *Biomaterials.* 35:961–969. http://dx.doi.org/10.1016/j.biomaterials.2013.10.037

Mertz, A.F., S. Banerjee, Y. Che, G.K. German, Y. Xu, C. Hyland, M.C. Marchetti, V. Horsley, and E.R. Dufresne. 2012. Scaling of traction forces with the size of cohesive cell colonies. *Phys. Rev. Lett.* 108:198101. http://dx.doi.org/10.1103/PhysRevLett.108.198101

Mertz, A.F., Y. Che, S. Banerjee, J.M. Goldstein, K.A. Rosowski, S.F. Revilla, C.M. Niessen, M.C. Marchetti, E.R. Dufresne, and V. Horsley. 2013. Cadherin-based intercellular adhesions organize epithelial cell-matrix traction forces. *Proc. Natl. Acad. Sci. USA.* 110:842–847. http://dx.doi.org/10.1073/pnas.1217279110

Monkley, S.J., X.H. Zhou, S.J. Kinston, S.M. Giblett, L. Hemmings, H. Priddle, J.E. Brown, C.A. Pritchard, D.R. Critchley, and R. Fässler. 2000. Disruption of the talin gene arrests mouse development at the gastrulation stage. *Dev. Dyn.* 219:560–574. http://dx.doi.org/10.1002/1097-0177(2000)9999:9999<::AID-DVDY1079>3.0.CO;2-Y

Notredame, C., D.G. Higgins, and J. Heringa. 2000. T-Coffee: A novel method for fast and accurate multiple sequence alignment. *J. Mol. Biol.* 302:205–217. http://dx.doi.org/10.1006/jmbi.2000.4042

Ochsner, M., M.R. Dusseiller, H.M. Grandin, S. Luna-Morris, M. Textor, V. Vogel, and M.L. Smith. 2007. Micro-well arrays for 3D shape control and high resolution analysis of single cells. *Lab Chip.* 7:1074–1077. http://dx.doi.org/10.1039/b704449f

Orr, A.W., B.P. Helmke, B.R. Blackman, and M.A. Schwartz. 2006. Mechanisms of mechanotransduction. *Dev. Cell.* 10:11–20. http://dx.doi.org/10.1016/j.devcel.2005.12.006

Pardee, J.D., and J.A. Spudich. 1982. Purification of muscle actin. *Methods Enzymol.* 85:164–181. http://dx.doi.org/10.1016/0076-6879(82)85020-9

Pasapera, A.M., I.C. Schneider, E. Rericha, D.D. Schlaepfer, and C.M. Waterman. 2010. Myosin II activity regulates vinculin recruitment to focal adhesions through FAK-mediated paxillin phosphorylation. *J. Cell Biol.* 188:877–890. http://dx.doi.org/10.1083/jcb.200906012

Plopper, G., and D.E. Ingber. 1993. Rapid induction and isolation of focal adhesion complexes. *Biochem. Biophys. Res. Commun.* 193:571–578. http://dx.doi.org/10.1006/bbrc.1993.1662

Plotnikov, S.V., A.M. Pasapera, B. Sabass, and C.M. Waterman. 2012. Force fluctuations within focal adhesions mediate ECM-rigidity sensing to guide directed cell migration. *Cell.* 151:1513–1527. http://dx.doi.org/10.1016/j.cell.2012.11.034

Priddle, H., L. Hemmings, S. Monkley, A. Woods, B. Patel, D. Sutton, G.A. Dunn, D. Zicha, and D.R. Critchley. 1998. Disruption of the talin gene compromises focal adhesion assembly in undifferentiated but not differentiated embryonic stem cells. *J. Cell Biol.* 142:1121–1133. http://dx.doi.org/10.1083/jcb.142.4.1121

Puklin-Faucher, E., and M.P. Sheetz. 2009. The mechanical integrin cycle. *J. Cell Sci.* 122:179–186. http://dx.doi.org/10.1242/jcs.042127

Ridley, A.J., and A. Hall. 1992. The small GTP-binding protein rho regulates the assembly of focal adhesions and actin stress fibers in response to growth factors. *Cell.* 70:389–399. http://dx.doi.org/10.1016/0092-8674(92)90163-7

Roca-Cusachs, P., T. Iskratsch, and M.P. Sheetz. 2012. Finding the weakest link: exploring integrin-mediated mechanical molecular pathways. *J. Cell Sci.* 125:3025–3038. http://dx.doi.org/10.1242/jcs.095794

Schiller, H.B., M.R. Hermann, J. Polleux, T. Vignaud, S. Zanivan, C.C. Friedel, Z. Sun, A. Raducanu, K.E. Gottschalk, M. Théry, et al. 2013. β_1- and α_v-class integrins cooperate to regulate myosin II during rigidity sensing of fibronectin-based microenvironments. *Nat. Cell Biol.* 15:625–636. http://dx.doi.org/10.1038/ncb2747

Solon, J., I. Levental, K. Sengupta, P.C. Georges, and P.A. Janmey. 2007. Fibroblast adaptation and stiffness matching to soft elastic substrates. *Biophys. J.* 93:4453–4461. http://dx.doi.org/10.1529/biophysj.106.101386

Srivastava, J., G. Barreiro, S. Groscurth, A.R. Gingras, B.T. Goult, D.R. Critchley, M.J. Kelly, M.P. Jacobson, and D.L. Barber. 2008. Structural model and functional significance of pH-dependent talin-actin binding for focal adhesion remodeling. *Proc. Natl. Acad. Sci. USA.* 105:14436–14441. http://dx.doi.org/10.1073/pnas.0805163105

Style, R.W., R. Boltyanskiy, G.K. German, C. Hyland, C.W. MacMinn, A.F. Mertz, L.A. Wilen, Y. Xu, and E.R. Dufresne. 2014. Traction force microscopy in physics and biology. *Soft Matter.* 10:4047–4055. http://dx.doi.org/10.1039/c4sm00264d

Turner, C.E., J.R. Glenney Jr., and K. Burridge. 1990. Paxillin: a new vinculin-binding protein present in focal adhesions. *J. Cell Biol.* 111:1059–1068. http://dx.doi.org/10.1083/jcb.111.3.1059

Volberg, T., B. Geiger, Z. Kam, R. Pankov, I. Simcha, H. Sabanay, J.L. Coll, E. Adamson, and A. Ben-Ze'ev. 1995. Focal adhesion formation by F9 embryonal carcinoma cells after vinculin gene disruption. *J. Cell Sci.* 108:2253–2260.

Wang, H.B., M. Dembo, and Y.L. Wang. 2000. Substrate flexibility regulates growth and apoptosis of normal but not transformed cells. *Am. J. Physiol. Cell Physiol.* 279:C1345–C1350.

Wehrle-Haller, B. 2012. Structure and function of focal adhesions. *Curr. Opin. Cell Biol.* 24:116–124. http://dx.doi.org/10.1016/j.ceb.2011.11.001

Xu, W., H. Baribault, and E.D. Adamson. 1998. Vinculin knockout results in heart and brain defects during embryonic development. *Development.* 125:327–337.

Zamir, E., B.Z. Katz, S. Aota, K.M. Yamada, B. Geiger, and Z. Kam. 1999. Molecular diversity of cell-matrix adhesions. *J. Cell Sci.* 112:1655–1669.

Zhang, X., G. Jiang, Y. Cai, S.J. Monkley, D.R. Critchley, and M.P. Sheetz. 2008. Talin depletion reveals independence of initial cell spreading from integrin activation and traction. *Nat. Cell Biol.* 10:1062–1068. http://dx.doi.org/10.1038/ncb1765

Ziegler, W.H., A.R. Gingras, D.R. Critchley, and J. Emsley. 2008. Integrin connections to the cytoskeleton through talin and vinculin. *Biochem. Soc. Trans.* 36:235–239. http://dx.doi.org/10.1042/BST0360235

Kumar et al., http://www.jcb.org/cgi/content/full/jcb.201510012/DC1

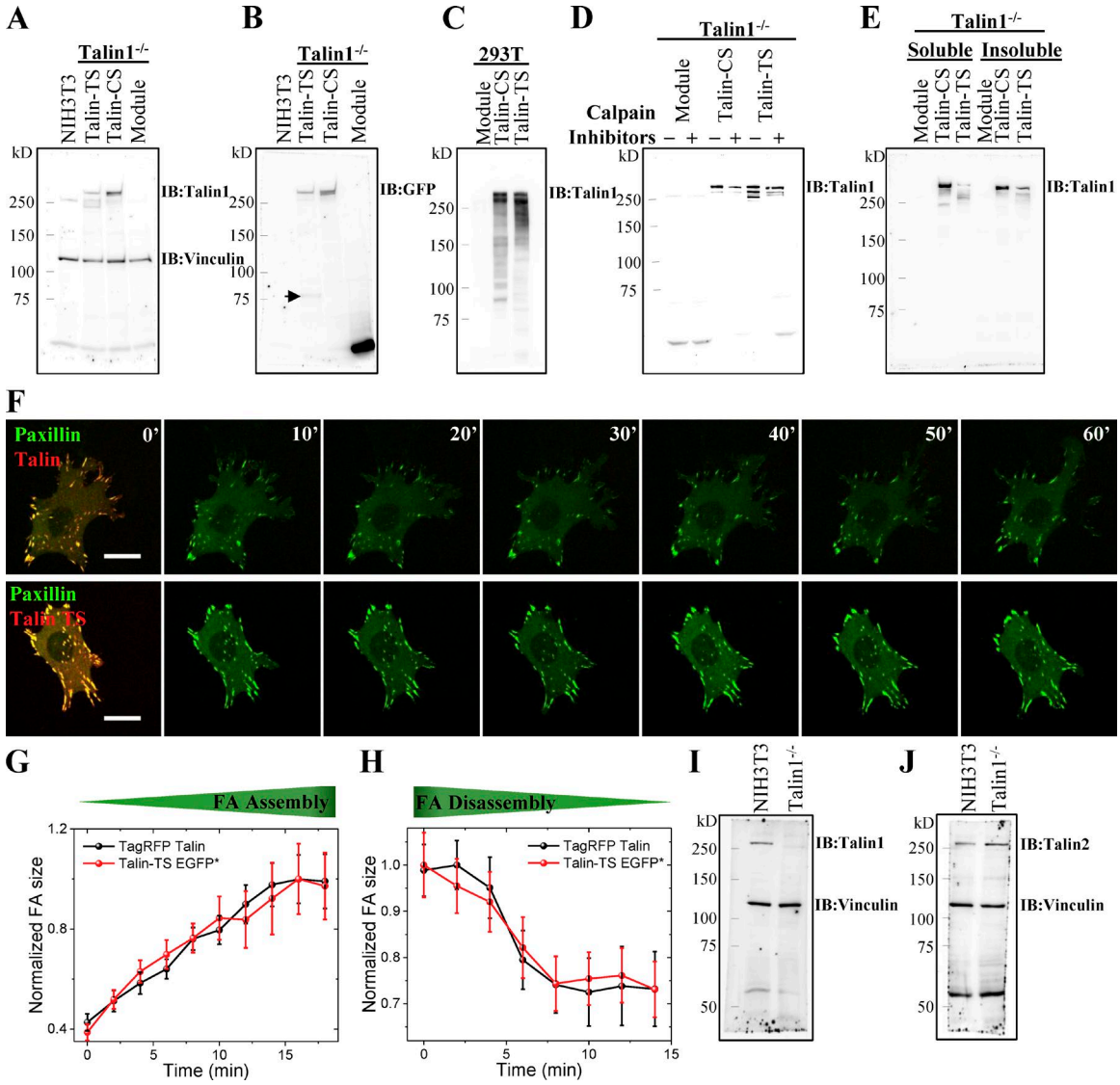

Figure S1. **Additional characterization of talin sensors in talin1$^{-/-}$ cells.** (A and B) Western blot for talin-TS and talin-CS in talin1$^{-/-}$ cells, probed for talin1 and vinculin (A) and stripped and reblotted with anti-GFP (B). The arrow indicates an ∼85-kD band. (C) Western blot of whole cell lysate of talin-CS– and talin-TS–transfected 293T cells, probed using talin1 antibody. (D) Western blot for talin-CS and talin-TS in talin1$^{-/-}$ cells without and with calpain inhibitors, probed with anti-talin1. (E) Western blot of soluble and insoluble protein after mild detergent extraction, probed with talin1 antibody. (F) Representative time-lapse images of talin1$^{-/-}$ cells cotransfected with paxillin EGFP and tagRFP talin (top) or tagRFP talin-TS (with nonfluorescent EGFP; bottom). (G and H) Plot of normalized FA size with time in assembling (n = 29 and 40; G) and disassembling (n = 37 and 47; H) FAs. Cells were freshly plated on fibronectin-coated dishes for ∼30 min before imaging. Low laser power was used, and only paxillin was imaged for time lapse to avoid phototoxicity. Cells were imaged for at least 60 min. Error bars represent SEM. Asterisks indicate mutations that destroy the fluorescence. (I and J) Western blot for talin1$^{-/-}$ cell lysate (control lane, NIH3T3 cell lysate) probed with talin1 (I) and talin2 antibodies (J). Bars, 20 µm. IB, immunoblot.

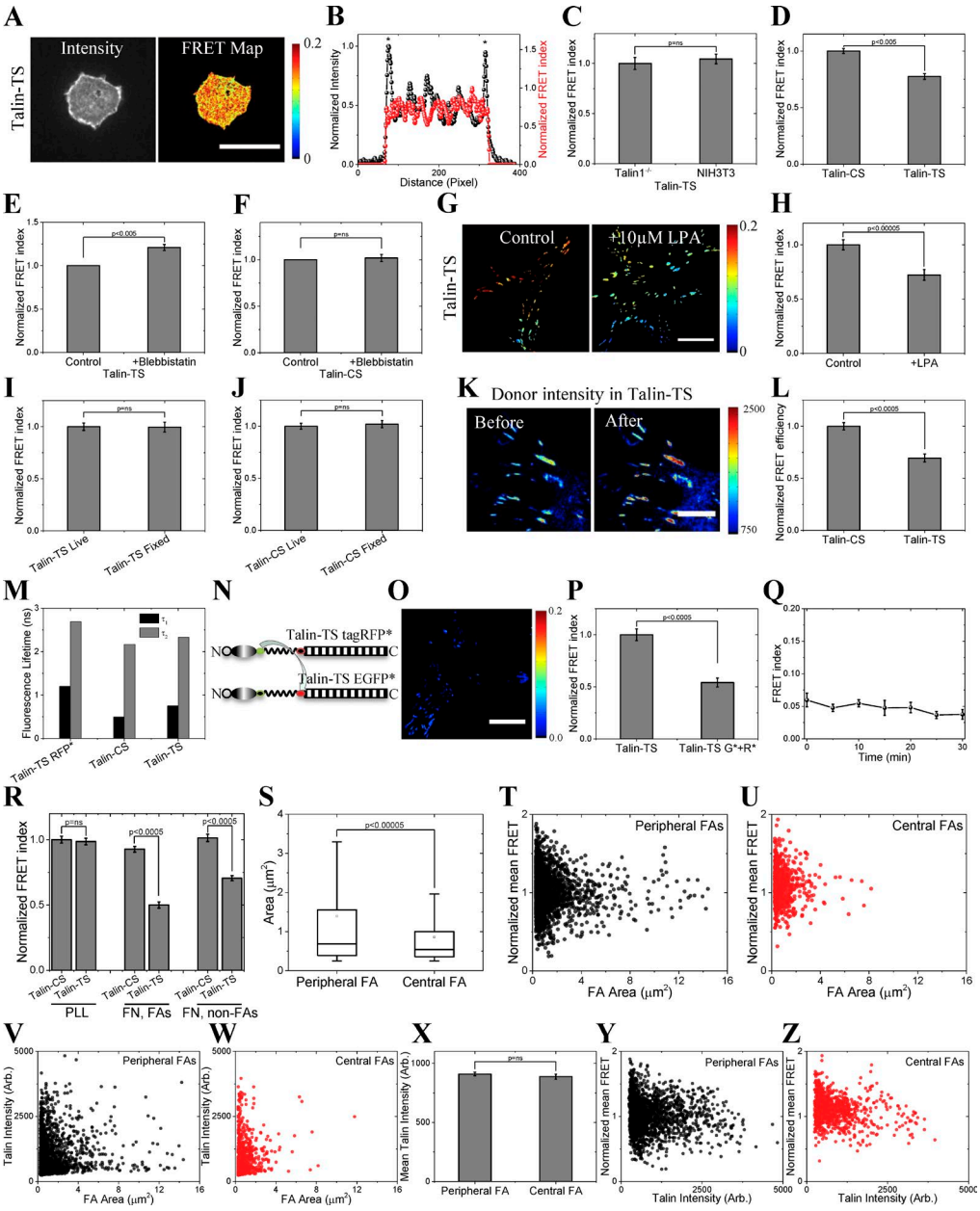

Figure S2. **Additional controls for talin-TS and differential tension on talin in peripheral and central FAs.** (A) Representative intensity and FRET map image of a talin-TS–transfected talin1$^{-/-}$ cell plated on poly-L-lysine; sections through the middle of the cell well above the substrate were analyzed. (B) Typical intensity line profile and FRET index profile across the cell. Asterisks denote plasma membrane–localized talin-TS. (C–F) Normalized FRET index of talin-TS in talin1$^{-/-}$ (n = 25) and NIH 3T3 cells (n = 25; C), talin-CS (n = 15) and talin-TS (n = 21) in NIH 3T3 cells (D), talin-TS before and after 5 µM blebbistatin treatment for 15 min (n = 6; E), and talin-CS before and after 5 µM blebbistatin treatment for 15 min (n = 14; F). (G) Representative FRET map of talin-TS in control and LPA-treated (10 µM for 30 min) cells serum starved in 0.2% FBS for 20 h. (H) Normalized FRET index for control (n = 25) and LPA-treated cells (n = 27). (I) Comparison of FRET index for talin-TS within FAs in live (n = 35) and fixed (n = 35) cells. (J) Comparison of FRET index for talin-CS within FAs in live (n = 29) and fixed (n = 28) in talin1$^{-/-}$ cells. (K) Pseudocolor map of donor intensity within FAs for talin-TS before and after acceptor photobleaching. (L) Normalized FRET efficiency for talin-CS (n = 30) and talin-TS (n = 44) within FAs measured by acceptor photobleaching. (M) Two-component fluorescence lifetime (τ_1 and τ_2) analysis of time domain data in talin-TS with nonfluorescent mutated tagRFP, talin-CS, and talin-TS. To fit the data, a biexponential model was used for all datasets, and the weighted mean lifetime was used for comparison. The global fitting method was used, in which the two lifetimes are kept constant across the members of a particular dataset, and the fractional contribution from each is allowed to vary between members of the same dataset, resulting in a spatially dependent weighted mean lifetime distribution. Hence, there are no error bars. (B and M) n > 60. (N) Schematic showing FRET between two talin-TS molecules containing mutated nonfluorescent EGFP and tagRFP. (O) Intermolecular FRET map of talin-TS within FAs. (P) Normalized intermolecular FRET index for talin-TS (n = 15 each). Asterisks indicate nonfluorescent mutants. (Q) Effect of 5 µM blebbistatin on intermolecular FRET within FAs (n = 5). (R) Normalized FRET index of cells expressing talin-CS and talin-TS, plated on poly-L-lysine (n = 20 and 15 for talin-CS and talin-TS, respectively). Alternatively, cells were plated on fibronectin, and the FRET index was measured within FAs (n = 29 and 35 for talin-CS and talin-TS, respectively) or in non-FA regions of the basal surface (n = 30 and 35 for talin-CS and talin-TS, respectively). (S) Plot of peripheral and central FA area. (T and U) Correlation between FA area and FRET index in peripheral (T) and central (U) FAs. (V and W) Correlation between FA size and talin intensity in FAs for peripheral (V) and central (W) FAs. (X) Mean talin intensity in peripheral and central FAs. (Y and Z) Correlation between normalized mean FRET index and talin intensity in peripheral (Y) and central (Z) FAs. (S–Z) n = 32. Bars: (A, G, and O) 20 µm; (k) 10 µm. Arb., arbitrary units. PLL, poly-L-lysine. FN, fibronectin. Error bars represent SEM, except for in S, where bottom and top error bars represent 5th and 95th percentiles, respectively.

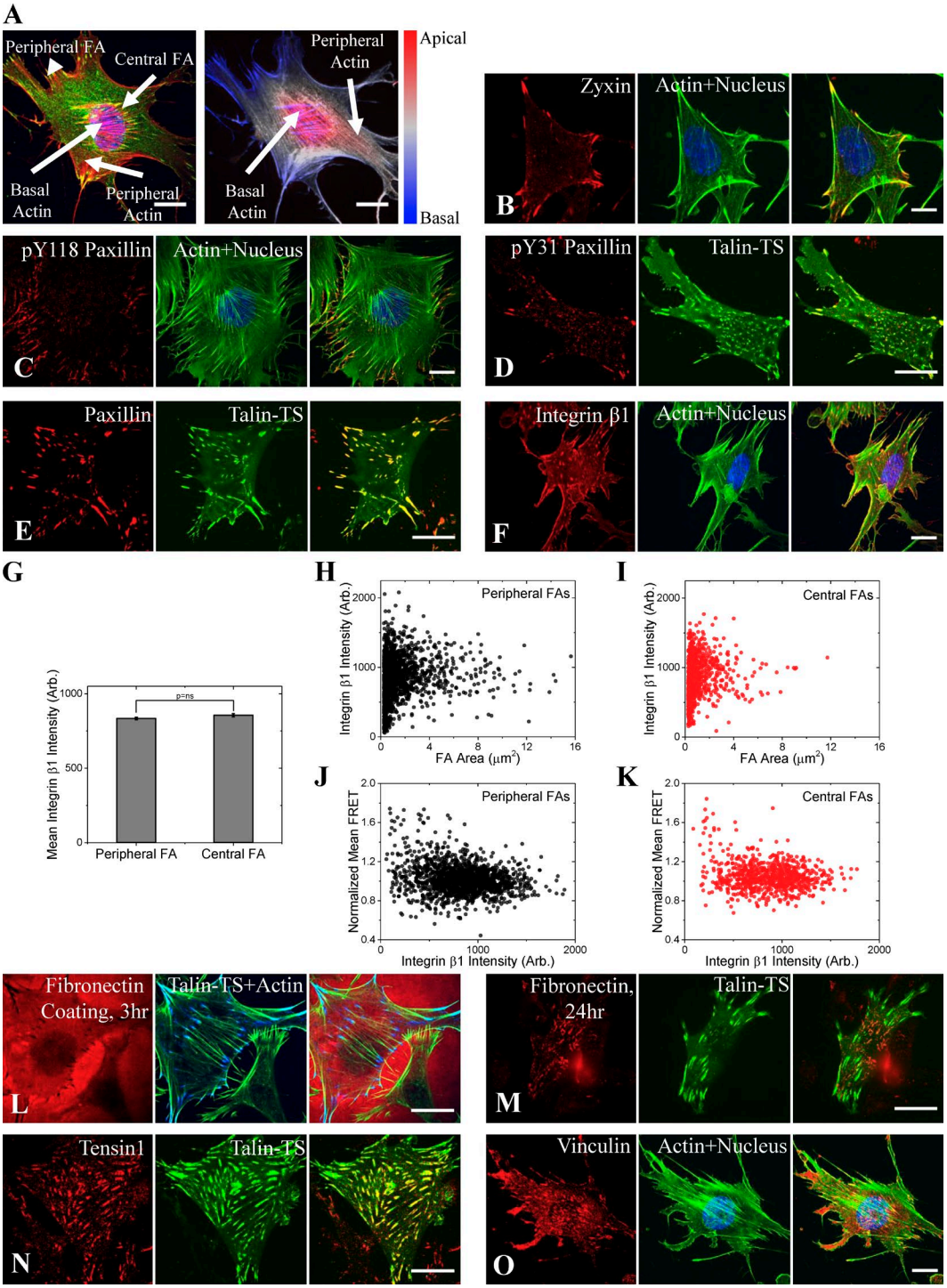

Figure S3. **Compositional difference in central and peripheral FAs.** (A) Central and peripheral actin and FAs, in which the z axis is color coded (right). (B–F) Immunofluorescence staining of zyxin (B), phospho-paxillin Y118 (C), phospho-paxillin Y31 (D), paxillin (E), and integrin β1 (F). (G) Mean intensity of integrin β1 in peripheral and central FA. *n* = 25 cells each. (H and I) Correlation between integrin β1 expression and FA area in peripheral (H) and central (I) FAs. *n* = 25 cells each. (J and K) Correlation between talin FRET index and integrin β1 expression in peripheral (J) and central (K) FAs. *n* = 25 cells each. (L–O) Immunofluorescence staining of fibronectin at 3 h after plating cells on fibronectin-coated dishes (L), fibronectin after 24 h of plating on an uncoated dish (M), tensin1 (N), and vinculin (O). Bars, 20 μm. Arb., arbitrary units.

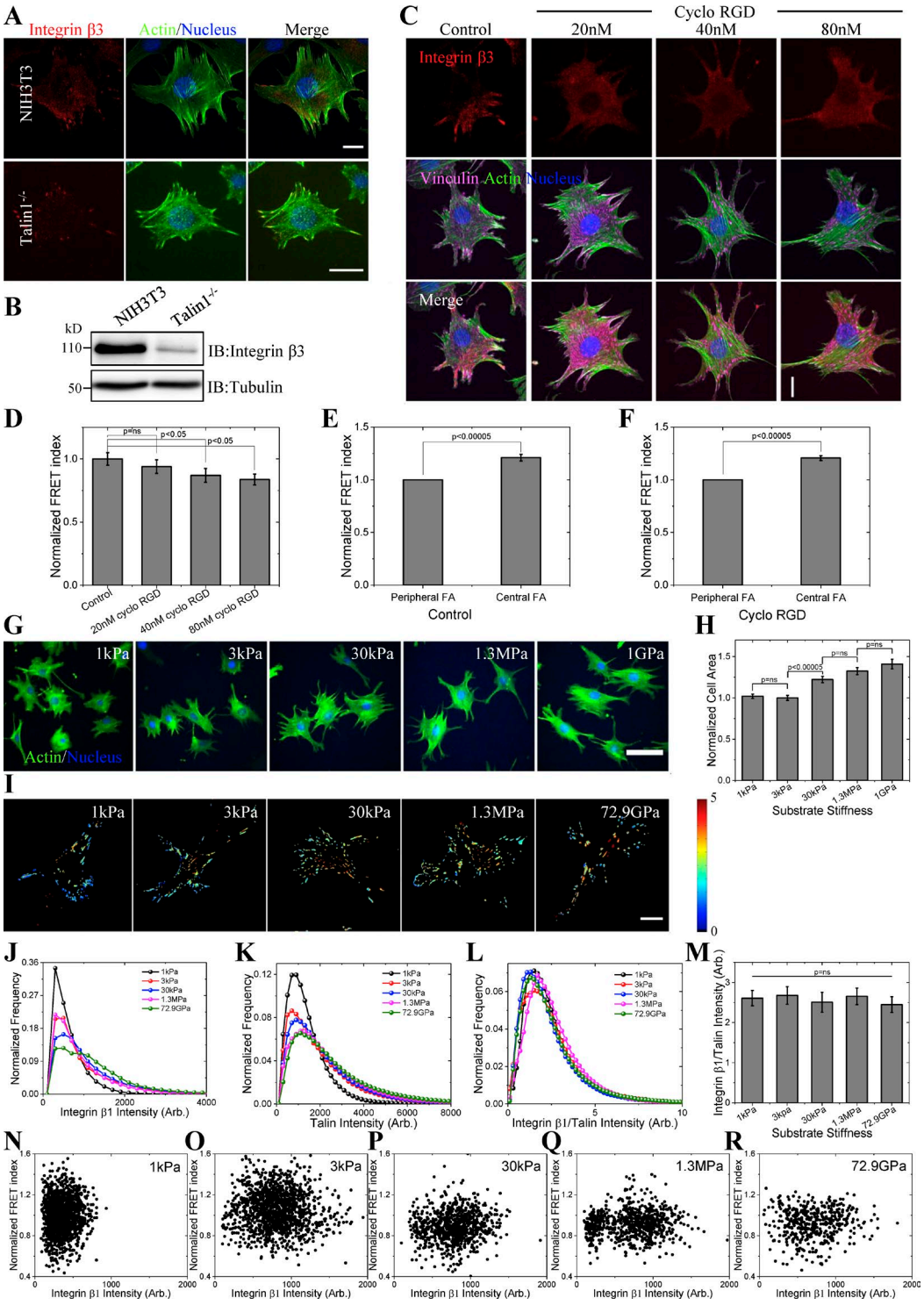

Figure S4. **Integrin β3 in central and peripheral FAs and amount of integrin β1 in FAs on substrates of different stiffness.** (A) Representative image of NIH 3T3 and talin1$^{-/-}$ cells immunostained for integrin β3 (red). Actin and nuclei are labeled in green and blue using phalloidin and Hoechst 33342, respectively. (B) Western blot for integrin β3. IB, immunoblot. (C) Representative image of integrin β3 immunostaining in NIH3T3 cells with cyclic RGD peptide (0 [control], 20, 40, and 80 nM) cyclo (Arg-Gly-Asp-D-Phe-Val). Vinculin, purple; actin, green; nucleus, blue. (D) Normalized FRET index of talin-TS in talin1$^{-/-}$ cells after cyclo RGD treatment (n = 25 in each case). (E and F) Normalized FRET index of talin-TS in peripheral and central FAs for talin1$^{-/-}$ cells in the control (n = 10; E) and treated with 80 nM cyclo RGD (n = 25; F). (G) Representative images of NIH 3T3 fibroblasts plated for 3 h on substrates of different stiffness that were coated with 10 µg/ml fibronectin (overnight) and then fixed and stained for actin and nucleus using Alexa Fluor 488–conjugated phalloidin and Hoechst 33342, respectively. (H) Plot of normalized cell area on these substrates (n = 126, 104, 93, 80, and 78 cells for 1 kPa, 3 kPa, 30 kPa, 1.3 MPa, and ∼1 GPa [plastic], respectively). (I) Representative ratio image of integrin β1/talin-TS intensity on substrates of different stiffness. (J–L) Pixel-wise intensity histogram for integrin β1 (J), talin-TS (K), and integrin β1/talin-TS intensity (L). (M) Mean integrin β1/talin-TS intensity (n = 22, 22, 25, 19, and 25 cells for 1 kPa, 3 kPa, 30 kPa, 1.3 MPa, and 72.9 GPa [glass], respectively). (N–R) Correlation between mean integrin β1 intensity and normalized talin FRET index on PDMS substrates of different stiffness. n = 9, 15, 9, 8, and 7 cells for 1 kPa (N), 3 kPa (O), 30 kPa (P), 1.3 MPa (Q), and glass (72.9 GPa; R), respectively. Bars: (A, C, and I) 20 µm; (G) 100 µm. Arb., arbitrary units.

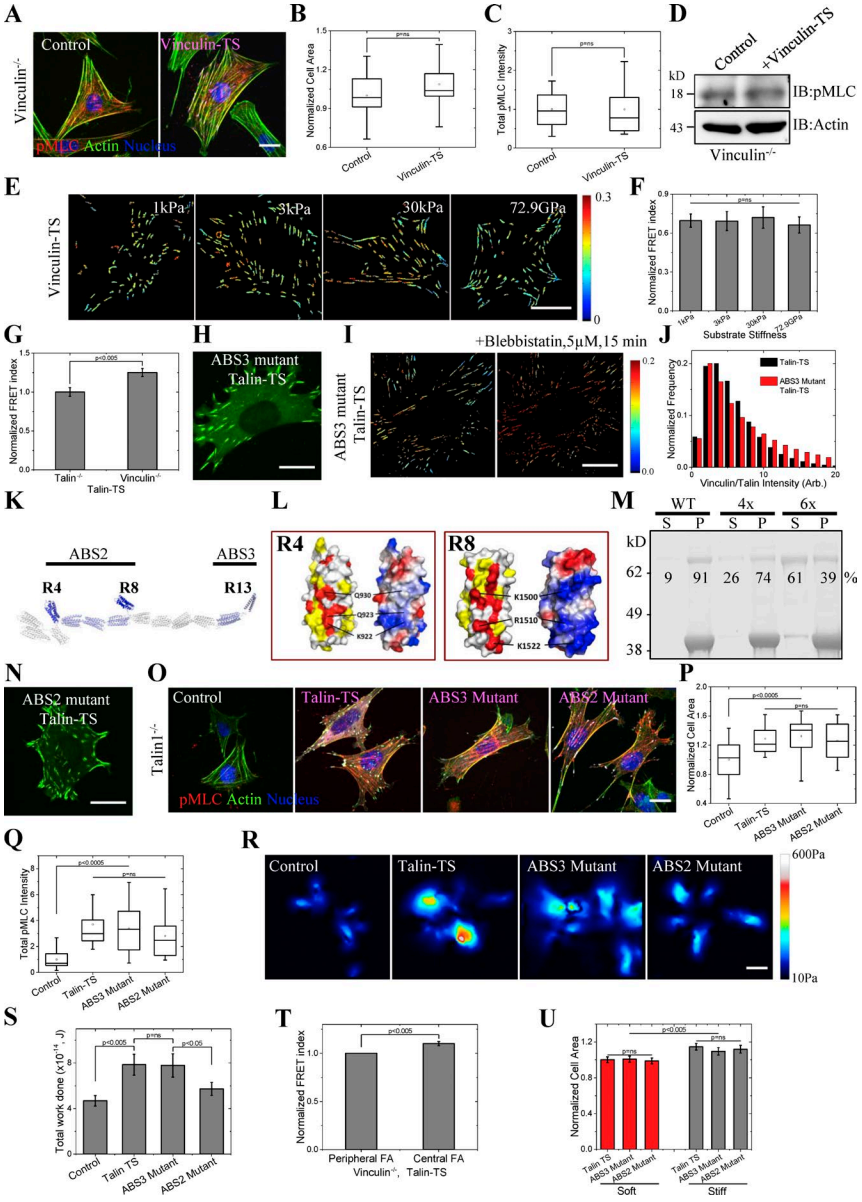

Figure S5. **Effect of stiffness on tension in vinculin and characterization of ABS2 mutant talin.** (A) Representative images of vinculin$^{-/-}$ cells, control and stably transfected with vinculin-TS (shown in purple). Cells were fixed and immunostained for phospho–myosin regulatory light chain (MLC; serine19; red). Actin (green) and nucleus (blue) were labeled using Alexa Fluor 568–phalloidin and Hoechst 33342, respectively. (B and C) Plot of normalized cell area (n = 24 and 25; B) and total phospho-MLC calculated from z-stack images captured with 0.5-μm z separation (n = 20 and 22; C) for control and vinculin-TS cells. (D) Western blot for phospho-MLC in the two cell lines. IB, immunoblot. (E) Representative FRET map of vinculin-TS stably transfected in vinculin$^{-/-}$ cells and plated on substrates of different stiffness. (F) Plot of mean FRET index for vinculin-TS, normalized by vinculin-TL for the corresponding substrate stiffness (n = 20, 20, 20, and 9 for 1 kPa, 3 kPa, 30 kPa, and 72.9 GPa [glass], respectively). (G) Normalized FRET index for talin-TS in talin1$^{-/-}$ (n = 25) and vinculin$^{-/-}$ (n = 25) cells. (H) Representative image of ABS3 mutant talin-TS in talin1$^{-/-}$ cells. (I) Representative FRET index map of ABS3 mutant talin-TS in talin1$^{-/-}$ cells before and after 5 μM blebbistatin treatment for 15 min. (J) Pixel-wise histogram for vinculin/talin ratio for talin-TS (n = 25) and ABS3 mutant talin-TS (n = 25) within FAs. Arb., arbitrary units. (K) Schematic diagram showing the location of the two ABSs (ABS2, residues 913–1653; and ABS3, residues 2300–2541) in the talin rod. The two R13 domains of the ABS3 dimer bind along one face of a single actin filament. The topologies of the R4 and R8 domains in ABS2 are similar to ABS3, and ABS2 may also wrap around single actin filaments. (L) Conservation (red is invariant and yellow is conservative substitutions) and surface charge characteristics of talin rod domains R4 and R8. The residues mutated in the 4× and 6× mutants are labeled. (M) Actin cosedimentation of talin ABS2. Talin fragments were incubated with F-actin, the actin was pelleted, and supernatants (S) and pellets (P) were analyzed by SDS-PAGE. WT, wild type. (N) Representative image of ABS2 mutant talin-TS transfected in talin1$^{-/-}$ cells. (O) Representative image of talin1$^{-/-}$ cells: control (untransfected), transfected with talin-TS, and ABS3 and ABS2 mutant talin-TS (shown in purple). Cells were fixed and immunostained for phospho-MLC (serine19; red). Actin (green) and nucleus (blue) were labeled using Alexa Fluor 568–phalloidin and Hoechst 33342, respectively. (P and Q) Plot of normalized cell area (n = 36, 20, 21, and 19; P) and total phospho-MLC calculated from z-stack images captured with 0.5-μm z separation (n = 36, 22, 23, and 25; Q) for untransfected control and talin-TS– and ABS3 and ABS2 mutant talin-TS–transfected talin1$^{-/-}$ cells. (R and S) Representative images of traction force field map (R) and plot of total work done (n = 15, 11, 14, and 11; S) for untransfected control and talin-TS– and ABS3 and ABS2 mutant talin-TS–transfected talin1$^{-/-}$ cells. (T) Normalized FRET index for talin-TS within central and peripheral FAs of vinculin$^{-/-}$ cells (n = 28). (U) Plot of normalized cell area on soft ~3-kPa (red bar; n = 50, 52, and 38) and stiff ~30-kPa (gray bar; n = 53, 40, and 33) substrate for talin-TS– and ABS3 and ABS2 mutant talin-TS–transfected talin1$^{-/-}$ cells. Bars, 20 μm. (B, C, P, and Q) Bottom and top error bars represent 5th and 95th percentiles, respectively. Small squares inside the box plots are the means. Box limits denote 25th and 75th percentiles. (F, G, and S–U) Error bars represent SEM.